

## A Quantitative Comparison of High Latitude Electric Field Models During a Large Geomagnetic Storm

L. Orr<sup>1,2</sup> , A. Grocott<sup>1</sup> , M.-T. Walach<sup>1</sup> , G. Chisham<sup>3</sup> , M. P. Freeman<sup>3</sup> , M. M. Lam<sup>3</sup> , and R. M. Shore<sup>3</sup> 

<sup>1</sup>Space and Planetary Physics, Lancaster University, Lancaster, UK, <sup>2</sup>Now at British Geological Survey, Edinburgh, UK,

<sup>3</sup>British Antarctic Survey, Cambridge, UK

### Key Points:

- The Heelis model is strongly dependent on the transpolar voltage proxy as input. The Kp based proxy is poor in storm time compared to others
- Models similar during quiet conditions but the spacecraft-based models are vastly different to the Super Dual Auroral Radar Network-based models during storm times
- As storm times are important for Joule Heating and satellite drag these differences must be considered by model users

### Supporting Information:

Supporting Information may be found in the online version of this article.

### Correspondence to:

L. Orr,  
lauren@bgs.ac.uk

### Citation:

Orr, L., Grocott, A., Walach, M.-T., Chisham, G., Freeman, M. P., Lam, M. M., & Shore, R. M. (2023). A quantitative comparison of high latitude electric field models during a large geomagnetic storm. *Space Weather*, 21, e2022SW003301. <https://doi.org/10.1029/2022SW003301>

Received 22 SEP 2022  
Accepted 12 DEC 2022

**Abstract** Models of the high-latitude ionospheric electric field (EF) are commonly used to specify the magnetospheric forcing in thermosphere or whole atmosphere models. The use of decades-old models based on spacecraft data is still widespread. Currently the Heelis et al. (1982, <https://doi.org/10.1029/ja087ia08p06339>) and Weimer (2005b, <https://doi.org/10.1029/2005ja011270>) climatology models are most commonly used but it is possible a more recent EF model could improve forecasting functionality. Modern EF models, derived from radar data, have been developed to incorporate advances in data availability (Bristow et al., 2022, <https://doi.org/10.1029/2021sw002920>; Thomas & Shepherd, 2018, <https://doi.org/10.1002/2018ja025280>; Walach et al., 2022, <https://doi.org/10.1029/2021ja029559>). It is expected that climatologies based on this larger and up-to-date data set will better represent the high latitude ionosphere and improve forecasting abilities. An example of two such models, which have been developed using line-of-sight velocity measurements from the Super Dual Auroral Radar Network (SuperDARN) are the Thomas and Shepherd model (TS18) (Thomas & Shepherd, 2018, <https://doi.org/10.1002/2018ja025280>), and Walach and Grocott geomagnetic Storm model (WGS21) (Walach et al., 2021, <https://doi.org/10.1029/2020ja028512>). Here we compare the outputs of these EF models during the September 2017 storm, covering a range of solar wind and interplanetary magnetic field (IMF) conditions. We explore the relationships between the IMF conditions and the model output parameters such as transpolar voltage, the polar cap size and the lower latitude boundary of convection. We find that the electric potential and field parameters from the spacecraft-based models have a significantly higher magnitude than the SuperDARN-based models. We discuss the similarities and differences in topology and magnitude for each model.

**Plain Language Summary** To prevent collisions between satellites and space junk within the Earth's space environment we need to accurately predict their position. The Ionosphere is part of the upper atmosphere of the Earth a which is affected by space weather events such as geomagnetic storms. Accurate ionospheric electric field models are key to accurate orbit prediction. Currently the use of decades-old models based on spacecraft data from the 80s is still widespread. We aim to compare the output from these commonly used spacecraft-based models to more recent models which were developed using line-of-sight velocity measurements from the Super Dual Auroral Radar Network (SuperDARN). We find that the parameters output from the spacecraft-based models often are significantly different to the SuperDARN-based models. We discuss the similarities and differences in topology and magnitude for each model.

## 1. Introduction

The high latitude ionospheric electric field (EF) is driven by coupling of the solar wind, magnetosphere and ionosphere. It is an integral part of space weather and can affect both ground-based and space-born technology; it is therefore important that we can accurately model the ionospheric EF. For example, the ionospheric EF is an important source of uncertainty in satellite drag and hence the risk of collisions between satellites and space debris. The EF causes ions and electrons to accelerate parallel to the EF and drift perpendicular to it such that they collide with neutral particles and heat the thermosphere. This Joule heating expands the thermosphere, causing the air density to locally increase and hence satellite drag.

One impact of the Space Weather Instrumentation, Measurement, Modeling and Risk: Thermosphere (SWIMMR-T) program aims to improve the UK's ability to specify and forecast the thermosphere. To do this, it is using and developing a physics-based, coupled thermosphere-ionosphere assimilative model for satellite drag and

© 2022. The Authors.

This is an open access article under the terms of the [Creative Commons Attribution License](https://creativecommons.org/licenses/by/4.0/), which permits use, distribution and reproduction in any medium, provided the original work is properly cited.

**Table 1**  
*List of Commonly Used Electric Field Models With Details Summarized*

ID	References	Time span	Solar cycle	Data source	Parameters	Grid	Lower boundary
H82	Heelis et al. (1982)				See Table S1 in Supporting Information	Analytical	Equator
HH90	Hairston and Heelis (1990)	08/1981–03/1983 (<100 passes)	SC21 (max.-declining phase)	DE-2	$\Phi_{PC}, B_y, -B_z$ only	Analytical, continuous, offset polar cap	Equator
W05	Weimer (2005b)	08/1981–03/1983 (2,064 passes)	SC21 (max.-declining phase)	DE-2	$B_y, B_z, n, V$ , tilt	Spherical cap harmonic analysis	4.2° offset circle with radius $R = f(\theta, B_{yc}, V, n)$ .
TS18	Thomas and Shepherd (2018)	2010–2016	SC24 (min.-declining phase)	Super-DARN (SD)	$E_{sw}, \theta_{clk}$ , tilt	SH cap fit where cap size is circle whose lowest latitude equals HMB	Min. latitude HMB with max. midnight latitude for merged vectors with $V > 150$ m/s for 25 + points adjacent to boundary
TS18 Kp	Thomas and Shepherd (2018)	2010–2016	As above	SD	Kp, $\theta_{clk}$	As above	As above
WGS21	Walach et al. (2021)	54 storms 2010–2016	As above	SD	Storm Phase: Sym-H	As above	The lower quartile (25%) of the HMBs from the original maps is used

Note. HMB, Heppner-Maynard boundary.

other applications called AENeAS (Advanced Ensemble electron density [Ne] Assimilation System) (Elvidge & Angling, 2019). AENeAS is based on the Thermosphere Ionosphere Electrodynamics General Circulation Model (TIEGCM; Dickinson et al., 1981) which requires an appropriate ionospheric EF model of which there are many models currently used routinely in space physics. Heelis et al. (1982) and Weimer (2005b) are two climatological models based on spacecraft data that are commonly used in modern atmospheric and space weather models. Currently TIEGCM and hence AENeAS interchangeably uses either a version of the Heelis et al. (1982) model, similar to that from M. Hairston and Heelis (1990), or the Weimer (2005b) model but it is possible that a “state-of-the-art” EF model will improve its functionality. Similarly, the Whole Atmosphere Community Climate Model With Thermosphere and Ionosphere Extension (WACCM-X) (Liu et al., 2018), is another General Circulation Model (GCM) which currently uses Heelis to specify the EF patterns, but Liu et al. (2018) suggests that the use of Weimer (2005b) or data assimilative schemes (Richmond & Kamide, 1988) would improve its simulations.

The Super Dual Auroral Radar Network (SuperDARN) (Chisham et al., 2007), a collection of ground-based coherent scatter radars, has been used for many years to measure and model ionospheric convection (Ruohoniemi & Baker, 1998). The addition of SuperDARN-based models could potentially help improve TIEGCM, AENeAS, WACCM-X and other modern GCMs by having an ionosphere model based on a spatially and temporally well sampled data set from the most recent solar cycle.

Table 1 summarizes the Heelis, Weimer, and SuperDARN family of models and highlights the similarities and differences between them. An important difference is the time interval of data on which each model is based, which is illustrated in Figure 1 in relation to the solar cycle and sunspot number. Figure 1 plots the previous four solar cycles (SC21–24) with shading showing the time range over which each of the models were devised. Weimer (2005b) and M. Hairston and Heelis (1990), denoted W05 and HH90 respectively, cover the 20 month period in the declining phase of SC21 for which Dynamics Explorer 2 (DE-2) was active. Ruohoniemi and Greenwald (1996) (RG96) covered most of SC22, Pettigrew et al. (2010) (PSR10) most of SC23, Cousins and Shepherd (2010) (CS10) the majority of SC23 and Thomas and Shepherd (2018) (TS18) and Walach et al. (2021) (WGS21) most of SC24.

Heelis et al. (1982) was originally a purely mathematical model for high latitude ionospheric convection based on Volland (1975). This model takes input parameters such as the radius of the convection reversal boundary, the

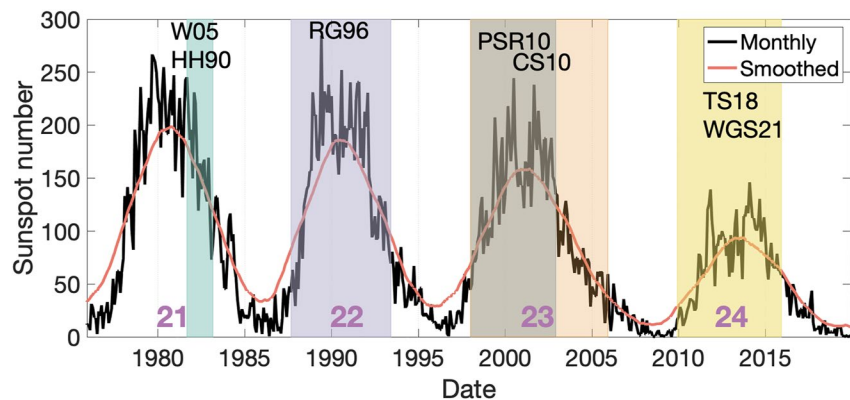


**Figure 1.** Monthly mean total sunspot number with W05, HH90, RG96, PSR10, CS10, WGS21 and TS18 time spans.

longitude of the dayside and nightside zero potential lines, and the magnitude of the maximum and minimum electric potentials. The full list of input variables are specified in Section S1 in Supporting Information S1.

This model was further developed by M. Hairston and Heelis (1990) such that the convection pattern was parameterized by the Interplanetary Magnetic Field (IMF)  $B_y$  and the transpolar voltage,  $\Phi_{PC}$ , only. They used data from DE-2, which operated between August 1981 and March 1983 in a polar orbit at altitudes of 300–1,000 km, to find relationships between the parameters in Heelis et al. (1982) with  $B_y$  and  $\Phi_{PC}$ . The DE-2 passes used in this analysis were limited to those starting and ending within 3 hr of magnetic local time (MLT) of the dawn-dusk meridian during intervals with IMF  $B_z$  negative. Fewer than 100 passes fulfilled those criteria.

The Weimer model (Weimer, 2005b) (W05) is a statistical electric potential model of the high-latitude ionosphere. Measurements of the ionospheric EF from more than 2,600 passes of the DE-2 satellite were used alongside solar wind and IMF conditions to create an empirical model of potential patterns. The model was developed from measurements of the electric potential variation along the satellite path estimated from the integration of EF components in the direction of motion. This model has been updated a number of times to increase spacecraft resolution, with the low-latitude boundary varying and improving the representation of the potentials using a combination of Fourier series and spherical harmonics (Weimer, 1995, 1996, 2001, 2005a). The model version utilized in this study (Weimer, 2005b) uses spherical cap harmonic analysis (SCHA) rather than Fourier fits around concentric bands. Input parameters include the IMF  $B_y$  and  $B_z$  components, the dipole tilt angle of the Earth, the solar wind velocity  $V$ , and the plasma number density  $n$ . Electric potential is calculated at different points in geomagnetic latitude and MLT, in AACGM (Altitude Adjusted Corrected Geomagnetic) coordinates.

Ruohoniemi and Greenwald (1996) were first to use line-of-sight  $E \times B$  velocity measurements from SuperDARN to derive a set of statistical electric potential patterns organized by IMF magnitude and clock angle. This “climatological” model was primarily built to augment instantaneous SuperDARN measurements in the SuperDARN fitting procedure known as Map Potential (Ruohoniemi & Baker, 1998). Map Potential uses all available SuperDARN line-of-sight velocity data at a given time to derive an instantaneous spherical harmonic solution of the electrostatic potential that is constrained by the statistical model in regions of no data coverage. Consequently the Map Potential solution tends toward the instantaneous measured data where it exists and toward the climatological model where the measurements are missing. Pettigrew et al. (2010) improved the climatological model by adding dipole tilt angle as a parameter and Cousins and Shepherd (2010) expanded the data set and added a dependence on solar wind velocity. Recently Thomas and Shepherd (2018) developed this model further using data from solar cycle 24, which exploited the expansion of SuperDARN radars to mid-latitudes ( $50^\circ$ – $60^\circ$ ) and to the polar cap ( $80^\circ$ – $90^\circ$ ). Their climatological electric potential patterns were organized by the solar wind EF magnitude ( $E_{sw}$ ), the IMF clock angle ( $\theta_{clk}$ ), and the dipole tilt angle. This is the model version currently used in Map Potential. Thomas and Shepherd (2018) further included a version of their climatology parameterized by the magnetic planetary “Kp” index and clock angle.

A new set of models being developed to improve ionospheric EF representation within atmospheric modeling aims to capture the time-dependence of the ionospheric EF response to solar wind driving. These “Time-Variable Ionospheric EF” (or TiVIE) models are based on the results of previous studies into the nature of the ionospheric

EF during varying levels of solar wind driving (Grocott & Milan, 2014), geomagnetic storms (Walach et al., 2021) and substorms (Grocott, Wild, et al., 2009; Grocott et al., 2010). Unlike previous SuperDARN-based models, which are based on instantaneous climatologies, TiVIE makes use of novel parameterizations to capture major sources of time-variability in the EF pattern. TiVIE combines SuperDARN data into superposed epoch analyses to model the EF using spherical harmonics for different time-varying scenarios via one of three modes. The Grocott and Milan (2014) mode is parameterized by the upstream solar wind conditions of IMF strength, clock angle and a solar wind steadiness timescale. This latter parameter allows for differences in the duration of a given state of solar wind driving to be captured. The Grocott, Badman, et al. (2009); Grocott et al. (2010) mode is parameterized by the universal time, magnetic latitude and local time, of a substorm onset. This allows for variability due directly to the substorm, that may be temporally decoupled from the solar wind driver, to be captured. Lastly, the Walach et al. (2021) mode (WGS21) is parameterized by geomagnetic storm phase using Sym-H to account for the variability introduced specifically by geomagnetic storms. This mode is based on a list of 54 storms from 2010 to 2016 (Walach & Grocott, 2019). Geomagnetic storms are a major source of variability that is not captured using instantaneous IMF parameterizations. Instead of the instantaneous IMF, this mode uses the normalized time within the initial, main, and recovery phases defined using the Sym-H index. SuperDARN measurements at each normalized time are then averaged over all storms to estimate the electric potential by a spherical harmonic fit.

It is worth noting that a number of other climatological EF models, constructed from data taken over several years, have been produced. For example, the Auroral energy Spectrum and High-Latitude Electric field variability (ASHLEY) uses bulk ion drift measurements from the Defense Meteorological Satellite Program (DMSP) satellites during the most recent solar cycle (Zhu et al., 2021). Haaland et al. (2007) used measurements of the electron drift velocity made by the Electron Drift Instrument (EDI) on the Cluster spacecraft and Lomidze et al. (2019) constructed a climatology of high-latitude cross-track ion drift using measurements from Swarm. They both made comparisons to other high latitude EF models including W05 (Weimer, 2005b) and the SuperDARN-based model RG05 (Ruohoniemi & Greenwald, 2005). Lomidze et al. (2019) found reasonable statistical agreement between W05 and the Swarm cross-track ion drifts whilst Haaland et al. (2007) found large differences in  $\Phi_{PC}$  during southward IMF. Both studies focused on climatological comparison so do not capture the differences occurring during extremes such as storm times.

In this paper we will quantitatively compare a set of four ionospheric EF models (HH90, W05, TS18, and WGS21 mode of TiVIE) for the 7–8 September 2017 geomagnetic storm. Choosing a storm interval allows us to test the models under extreme driving conditions when space weather impacts will be greatest and when we might expect the models to be most deficient and diverse due to their limited input data set. It also enables us to contrast models based on typical data with the WGS21 model that is specifically tailored to storm times. Although we have chosen a single event, the storm we have picked nonetheless encompasses a variety of solar wind driving conditions and thus a range of input parameterization to the models, and there is good SuperDARN data coverage throughout the main phase of the storm. Performing an event-based comparison, rather than a statistical study avoids the complication introduced by the models having different input parameters (see Table 1). For example, TS18 is parameterized by solar wind EF  $E_{sw}$  and clock angle  $\theta_{clk}$ , whereas W05 is parameterized by solar wind speed  $V$  and IMF  $B_y$  and  $B_z$  components. Consequently, the TS18 and W05 statistical model outputs cannot be uniquely compared because a given  $E_{sw}$  and  $\theta_{clk}$  state can in general arise from different combinations of  $V$ ,  $B_y$ , and  $B_z$ , whereas a given event naturally selects all parameter values. Event-based comparison also allows us to compare the model outputs to the SuperDARN Map Potential output as a “ground-truth” data set, recognizing that we are comparing this “ground-truth” to both SuperDARN and non-SuperDARN models.

In Section 2 we describe the method, the model versions and the data used, Section 3 shows the results and Section 4 discusses the findings.

## 2. Methods

### 2.1. Model Versions

The models used in this study are summarized in Table 1. The version of the Heelis model used for the analysis in this paper is taken from TIEGCM (Qian et al., 2014) within AENeAS (Elvidge & Angling, 2019; HAO, 2018). A full description of the code is included in the SI but we will refer to it as HH90 due to its similarities with

M. Hairston and Heelis (1990). The W05 model is described by Weimer (2005b) and was provided by Daniel Weimer. TS18 (Thomas & Shepherd, 2018) is available as part of the Radar Software Toolkit (RST (4.4.1)) (SuperDARN Data Analysis Working Group et al., 2021). WGS21 (Walach et al., 2021) is available from Lancaster University's research archive (PURE).

## 2.2. Selection of Event

The chosen interval of interest is from 20:00 UT on 7 September to 03:20 UT on 8 September. The interval is within a geomagnetic storm, as shown in Figure S1 in Supporting Information S1 by the characteristic rapid decrease in the Sym-H index and slow recovery. The minimum Sym-H is  $-146$  nT, which defines this event as an intense storm ( $-250$  nT < minimum Sym-H <  $-100$  nT).

Following the definition of storm phases devised by Walach and Grocott (2019) for the WGS21 mode of the TiVIE model, the storm begins at 11:02 UT on 7 September and ends at 18:40 UT on 10 September. Within this, the storm's initial phase is from 11:02 to 23:07 UT on 7 September, the main phase then follows until 01:08 UT on 8 September, and thereafter the recovery phase until the storm end at 18:40 UT on 10 September. It should be noted that the Walach and Grocott (2019) definition of the start of a storm is not based on the Sudden Storm Commencement (SSC), as is commonly the case. Instead, it is the start of a storm initial phase that is defined as a quiet interval ahead of the storm main phase in which Sym-H maximizes and is greater than  $-15$  nT. The Walach and Grocott definition is more practical for storms without an SSC or due to the interaction of multiple solar ejecta, as is the case in this storm (Dimmock et al., 2019). The 7 hr 20 min interval within the storm has been selected to include the 2 hr 3 min main phase from 23:07 UT (7th) to 01:10 UT (8th) and similar length intervals of the surrounding initial and recovery phases.

## 2.3. Model Input Control Variables

As mentioned in the Introduction, the decision to use a single event to compare the models is because they each have different control variables as input (see Table 1) which cannot be uniquely related to each other. For example, (a) TS18 has 120 climatological patterns for different combinations of inputs  $E_{sw}$ ,  $\theta_{clk}$ , and dipole tilt angle (where  $E_{SW} = |V_x| \sqrt{B_y^2 + B_z^2}$  and  $\theta_{clk} = \arctan\left(\frac{B_y}{B_z}\right)$ ), (b) W05 input control variables includes IMF  $B_y$ ,  $B_z$ , the dipole tilt angle of the Earth, solar wind velocity,  $V$ , and plasma number density,  $n$ . (c) HH90 takes  $\Phi_{PC}$  and IMF  $B_y$  as input control variables, and (d) WGS21 uses only storm phase and normalized time within it.

Considering first the WGS21 model, the ionospheric EF is defined in this model for each time step within the initial, main, and recovery phases at 2 min cadence. The duration of these phases are defined in the model to be 587, 272, and 1,673 time steps, respectively, corresponding to the average length in minutes of these phases for the 54 storms on which the model is based. For the September 2017 storm event studied here, the duration of the initial, main and recovery phases are found to be 725, 121, and 3,932 min, respectively. Thus the model time step in each phase is scaled by the ratio of the event phase duration to the model phase duration, that is,  $725/587 = 1.24$  min,  $121/272 = 0.445$  min, and  $3,932/1,673 = 2.35$  min for the initial, main, and recovery phases, respectively. Consequently, for the interval of interest from 20:00 UT on 7 September to 03:20 UT on 8 September, we use the final 151 of the 587 time steps of the model initial phase, all 272 time steps of the model main phase, and the first 57 of the 1,673 time steps of the model recovery phase, making a total of 480 model time steps.

For the W05 and TS18 models, the interplanetary input control variables are provided by, or derived from, measurements from the ACE (Advanced Composition Explorer) and WIND spacecraft in the high resolution OMNI data set of the NASA Geophysical Data Center (GSFC/SPDF et al., 2021a). The database has been averaged at 1 min cadence such that our time interval of interest has 441 time points. The online database has been time lagged to the bow shock nose using methods specific to the spacecraft (Farris & Russell, 1994; Shue et al., 1997) as described in (GSFC/SPDF et al., 2021b). We then added a further time lag from the bow shock to the magnetopause based on an estimation of the subsolar magnetosheath transit time from Khan and Cowley (1999).

In the HH90 model, the input control variables are IMF  $B_y$ , which is available from OMNI, and the transpolar cap voltage  $\Phi_{PC}$ , which is a property of the ionospheric EF (see Section 2.4) and hence usually a model output variable. Therefore we need an equation to relate  $\Phi_{PC}$  to IMF and solar wind conditions, or other OMNI measurements. Five such equations are listed below:

### 2.3.1. Lockwood Equation

Lockwood and McWilliams (2021) recently used more than 65,000 hourly averages of  $\Phi_{PC}$  determined from over 25 years of SuperDARN radar observations to estimate the “optimum” solar wind-magnetosphere coupling function.

$$\Phi_L = B_{YZ}^{0.64} \rho_{SW}^{0.02} V_{SW}^{0.55} \sin^{2.5}(\theta_{clk}/2) \quad (1)$$

where  $B_{YZ}$  is the transverse component of the IMF, perpendicular to the Sun-Earth line.  $\rho_{SW}$  is the mass density,  $V_{SW}$  the solar wind speed, and  $\theta_{clk}$  is the clock angle (Lockwood & McWilliams, 2021). Each of these parameters are available at 1 min resolution at the bow shock from OMNI, hence  $\Phi_L$  can be calculated at 1 min cadence, with the lag from the bow shock nose to the magnetosphere added.

### 2.3.2. Kp

The equation currently used within TIEGCM and AENeAS (HAO, 2018) is a relationship with Kp. This is a 3-hr index provided as part of the Low Resolution OMNI (LRO) data set by the German Research Center for Geosciences (GFZ, Potsdam).

$$\Phi_{Kp} = 15 + 15Kp + 0.8Kp^2 \quad (2)$$

An obvious problem with this estimation is that the  $K_p$  index has a cadence of 3 hr and therefore  $\Phi_{Kp}$  does not capture smaller-scale temporal variations. Kp values are supplied every 3 hr, beginning at midnight, and we will use the most up-to-date Kp value at each subsequent time step. Unlike solar wind data which is measured upstream, Kp is not well forecast so is not as useful for a forecasting model. A simplified version of this equation appears in Boyle et al. (1997). According to Boyle et al. (1997) Kp provides a reasonable estimate of  $\Phi_{PC}$  if the IMF has been steady for several hours.

### 2.3.3. Polar Cap Index

Ridley and Kihn (2004) show a seasonal trend in the relationship between the Polar Cap Index (PCI) and transpolar voltage, and define a proxy  $\Phi_{PCI}$ :

$$\Phi_{PCI} = 19.28 - 3.31\sin(T + 1.49) + 17.81PCI, \quad (3)$$

$$T = (\text{month} - 1) \times 2\pi/12 \quad (4)$$

where *month* is the month of the year (i.e., January is *month* = 1) and PCI is available as OMNI data. Therefore, this equation is directly comparable to the TS18 and W05 models. It is available at a 1-min cadence but like Kp it is not available in advance, so cannot be used for forecasting.

### 2.3.4. Boyle Equation

$$\Phi_B = 10^{-4}V^2 + 11.7B\sin^3(\theta_{clk}/2) \quad (5)$$

which is defined such that  $\Phi_B$  is the transpolar voltage in kV,  $V$  is the solar wind bulk velocity in km/s,  $B$  is the IMF magnitude in nT and  $\theta_{clk}$  is the IMF clock angle (Boyle et al., 1997).

### 2.3.5. Milan Equation

$$\Phi_D = L_{eff}(V_x)V_xB_{YZ}\sin^{9/2}\frac{1}{2}\theta_{clk}, \quad (6)$$

$$L_{eff}(V_x) = 3.8\left(\frac{V_x}{4 \times 10^5}\right)^{1/3} \quad (7)$$

where  $\Phi_D$  is the dayside reconnection rate,  $V_x$  is the solar wind speed and  $B_{YZ}$  is the magnitude of the projection of the IMF vector in the  $Y$ - $Z$  GSM plane (Milan et al., 2012).

Some studies have used  $\Phi_{PC}$  as a proxy for dayside reconnection rate (Grocott, Badman, et al., 2009; P. H. Reiff et al., 1981; P. Reiff et al., 1985). Milan et al. (2012) suggests two flaws in this method. (a) Viscous interaction of the solar wind and the magnetosphere can cause convection without dayside reconnection. (b) The relationship between the two parameters is complex. The intervals used in Milan et al. (2012) had good representation of all clock-angles and values of  $B_{YZ}$  up to 12 nT and solar wind dynamic pressure up to 12 nPa, but few beyond. One issue identified in our results below is very high values of  $\Phi_D$  during storm time intervals. Milan et al. (2012) concludes that it is important to extend the observations to investigate the reconnection rate during extreme events. This could result in the proxy being better constrained during strong  $B_{YZ}$ .

## 2.4. Model Output Metrics

To quantitatively compare the models we produce time series of various model metrics that can be extracted from the modeled electric potentials as follows:

### 2.4.1. The Transpolar Voltage

$$\Phi_{PC} = \Phi_{\max} - \Phi_{\min}, \quad (8)$$

where  $\Phi_{\min}$  and  $\Phi_{\max}$  are the minimum and maximum electric potentials, respectively. We note that this may not represent the true transpolar voltage if the maximum and minimum potentials are not located at the foci of the dawn and dusk Dungey-cycle convection cells, respectively.

### 2.4.2. The Polar Cap Residual

$$\Phi_{res} = \Phi_{\max} + \Phi_{\min} \quad (9)$$

These two equations provide measures of the strength of the convection and the asymmetry between the dawn and dusk convection cells, respectively.

### 2.4.3. Mean Polar Electric Field

The mean EF magnitude,  $|\bar{EF}|$ , above  $60^\circ$  magnetic latitude, measured in mV/m.

$$|\bar{EF}| = \sum_{\theta, \psi} \frac{|EF|}{N}, \quad (10)$$

where  $\theta \geq 60^\circ$  represents the Altitude Adjusted Corrected GeoMagnetic (AACGM-v2) latitude,  $\psi$  represents all magnetic longitudes, and  $N$  is the number of points. This metric is the mean EF magnitude above  $60^\circ$  magnetic latitude, measured in mV/m. It allows us to include a measure of the mean strength of the convection for HH90, where  $\Phi_{PC}$  is an input and thus contains limited information about the model performance.

The EF is calculated using code adapted from part of the Heppner-Maynard-Rich EF Model 1990 (J. P. Heppner, 1977; J. Heppner & Maynard, 1987; Rich & Maynard, 1989). The north-south component of the EF is calculated at a point,  $\Phi_i$ , by taking the difference of the potential at the point to the north,  $\Phi_{i+1}$ , and the potential at the point to the south,  $\Phi_{i-1}$ , divided by the geographic distance between the two points. The east-west component of the EF is found in the same way by taking the gradient between a point to the east and west of a point in geographical coordinates.

### 2.4.4. Polar Cap Radius

A proxy for the radius of the polar cap,  $r_{pc}$ , is given by

$$r_{pc} = \frac{1}{2}(\theta_{\max} + \theta_{\min}) \quad (11)$$

where  $\theta_{\max}$  is the colatitude of the location of maximum potential and  $\theta_{\min}$  is the colatitude of the location of minimum potential. This measure is a proxy for the radius of the polar cap, with the same caveats as for the transpolar potential.

#### 2.4.5. Low Latitude Boundary

A “Heppner-Maynard boundary” (HMB) (J. Heppner & Maynard, 1987) is routinely determined for all SuperDARN models as the lower-latitude limit of the convection (see Table 1). The latitude of this boundary at midnight MLT is specified when performing the spherical harmonic fit. In W05, the low latitude boundary (LLB) is defined by an offset circle (Weimer, 2005a, 2005b). For comparison to the SuperDARN models we will take the value of the W05 LLB at midnight. In HH90 there is no defined LLB. Instead, equatorward of the polar cap boundary, the HH90 electric potential is described by a function that decreases exponentially with decreasing latitude (M. Hairston & Heelis, 1990). For purposes of comparison we will define the HH90 LLB as the latitude (at midnight) across which the mean electric potential drops below 0.418 kV, which is the mean electric potential of the LLB for W05 throughout the time period 7 September 20:00 UT to 8 September 03:20 UT. A different choice of LLB for HH90 would result in differences to Figure 2 panel I and Figure 7.

### 3. Results

#### 3.1. Parameterized Time Series of the September 2017 Storm

In Figure 2 we present a quantitative comparison of convection pattern parameters produced by the different models for a time period from 20:00 UT on the 7 September to 03:20 UT on the 8 September 2017, allowing for a range of IMF conditions during the initial, main and recovery phases of the storm. The start and end times of the main phase, as found from Sym-H using the method of Walach and Grocott (2019), are shown by the vertical, dashed gray lines at 23:07 UT on 7 September and 01:08 UT on 8 September. The parameters in Figure 2 are listed in Section 2.4. The vertical, dashed blue lines correspond to the snapshots in Figure 3.

Panel A shows the IMF parameters  $B_y$  and  $B_z$  in blue and orange, respectively. The horizontal, dashed line indicates 0 nT. The time interval chosen displays a range of IMF conditions, with positive and negative  $B_y$  and  $B_z$  plus a range of IMF clock angles. Panel B shows the Sym-H index which is used to define the storm phases (vertical, gray lines) as mentioned above. Panel C shows the number of SuperDARN vectors that were available at each time point, included to identify to what extent the Map Potential is relying on the TS18 model to infill the data gaps. The line-of-sight vectors are combined into cells of an equal area polar grid of spatial resolution  $\sim 110 \times 110$  km. The number of vectors are then the number of these gridded cells which are occupied by line-of-sight vectors. When the number of available vectors is low, Map Potential relies on TS18 to fill the data gaps. The number of vectors is low throughout the initial phase but increases to  $\sim 500$  vectors through the peak of the storm.

Panel D shows the transpolar voltage proxies from Section 2.3 Equations 1–7. Through the initial phase, whilst IMF  $B_z > \sim -10$  nT, all five proxies perform similarly with values between 100 and 180 kV. When  $B_z$  drops further the IMF and solar wind based proxies,  $\Phi_B$  and  $\Phi_D$  (Equations 5 and 7), reach huge values of 416 and 631 kV respectively.  $\Phi_L$  (Equation 1) has a more conservative but still high value of 337 kV. The PCI proxy,  $\Phi_{PC}$  (Equation 4) reaches 306 kV, while the Kp proxy,  $\Phi_{Kp}$  (Equation 2) only reaches 186 kV; Kp is a three-hourly index and so lacks the higher-resolution detail that is observed in the other three proxies that use 1-min IMF data. In the following panels E–H we use the proxies  $\Phi_L$  (Equation 3) and  $\Phi_{Kp}$  (Equation 2) as the  $\Phi_{PC}$  input for HH90.

Panel E shows the transpolar voltage,  $\Phi_{PC}$ , the difference between the maximum and minimum electric potential (Equation 8) for WGS21, TS18, W05 and Map Potential, as well as the  $\Phi_L$  and  $\Phi_{Kp}$  proxies used in HH90. Considering first the spacecraft-based models, HH90 ( $\Phi_L$ ) follows a similar trend to W05 throughout the storm but reaches a higher peak of 337 kV at 23:38 UT on the 7th compared to 256 kV for W05. HH90 ( $\Phi_{Kp}$ ) remains relatively steady at 180–190 kV throughout the main phase and for 2 hr before and after it, due to its low 3-hr resolution as already noted in reference to panel D. For the SuperDARN-based models  $\Phi_{PC}$  is significantly lower. The WGS21 values are elevated throughout the main phase, maximizing at 141 kV. TS18 saturates at  $\sim 90$  kV when  $B_z = -7$  nT from  $\sim 20:50$  UT and does not change significantly when IMF  $B_z$  continues to decrease. This is because the model is at its maximum  $E_{sw}$  bin where the model electric potential is averaged over all  $E_{sw} > 3$  mV/m. The Map Potential variation lies between WGS21 and TS18. It shows more variation than TS18 and reaches a higher maximum of 124 kV. Map potential tends toward the TS18 model when the number of vectors is low as

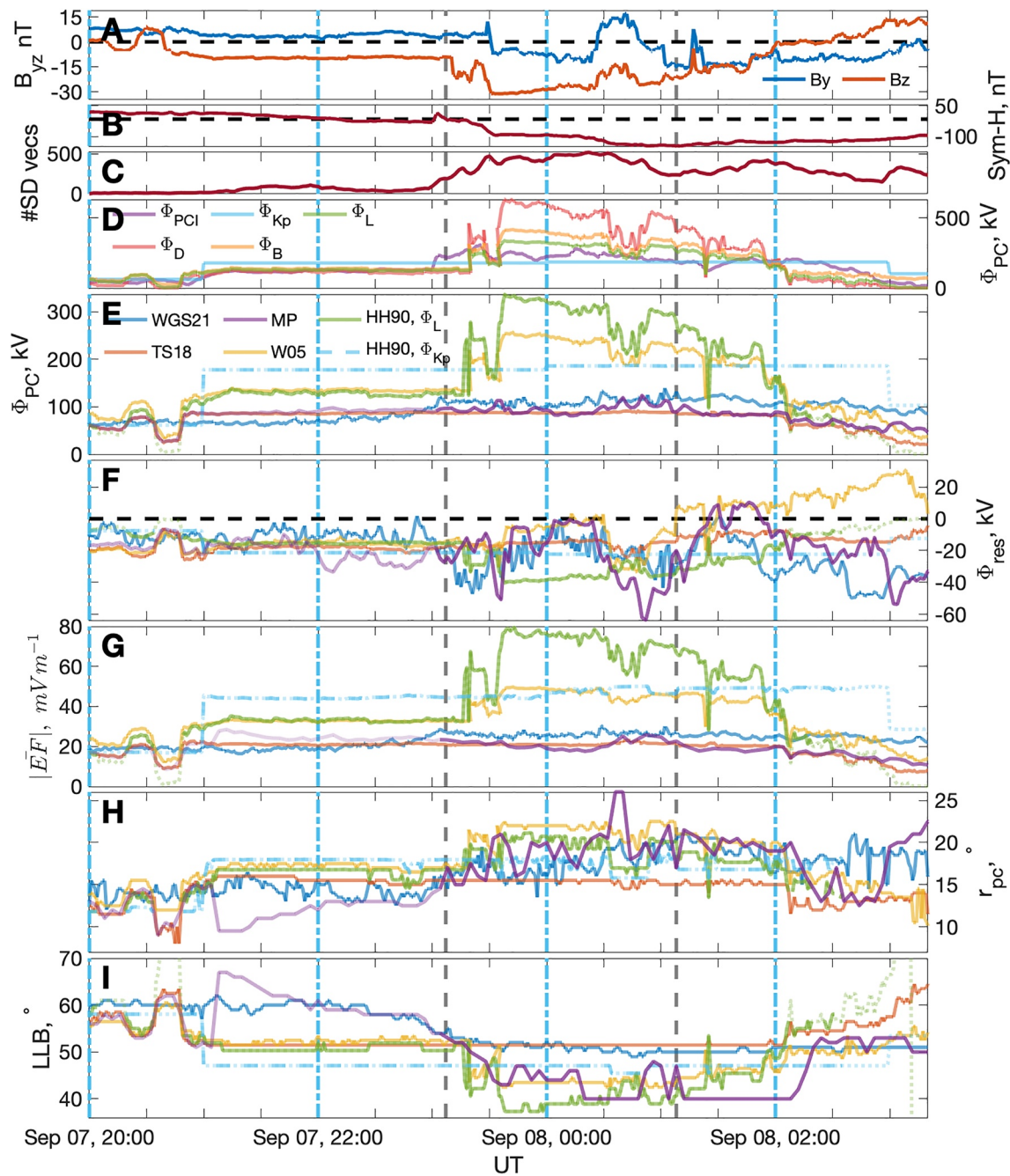


**Figure 2.** Panel A shows  $B_y$  (blue) and  $B_z$  (orange), panel B shows Sym-H, panel C the number of SuperDARN vectors available for the Map Potential, panel D shows five proxies for transpolar voltage,  $\Phi_{PC}$  which are given as Equations 2–7. Panel E plots the model outputs for  $\Phi_{PC}$  from WGS21, TS18, W05, and Map Potential. The models are each represented by the same set of colors in Panels D–I Where Map Potential is calculated from  $<100$  vectors is plotted in lighter purple. Panel F shows  $\Phi_{res}$  for the models as in Equation 9. Panel G shows the mean electric field above  $60^\circ$  as calculated using Equation 10. Panel H and I shows a proxy for the size of the polar cap and lower latitude boundary per model, respectively as calculated in Section 2.4. Vertical dashed blue lines match the snapshots from Figure 3. Vertical dashed gray lines represent the start and end of the main phase.

the model increasingly relies on the TS18 background model to infill data gaps. When there are few SuperDARN vector measurements available ( $<100$ ), the Map Potential parameter is shown in a lighter shade of purple.

Panel F is the residual of the potential, the sum of the maximum and minimum potential (Equation 9), which we use as a measure of asymmetry between the dawn and dusk cells. If  $\Phi_{res} < 0$ , the dusk cell has a stronger magnitude whilst if  $\Phi_{res} > 0$  the dawn cell is stronger. Through the main phase of the storm the dusk cell ( $\Phi_{min}$ )

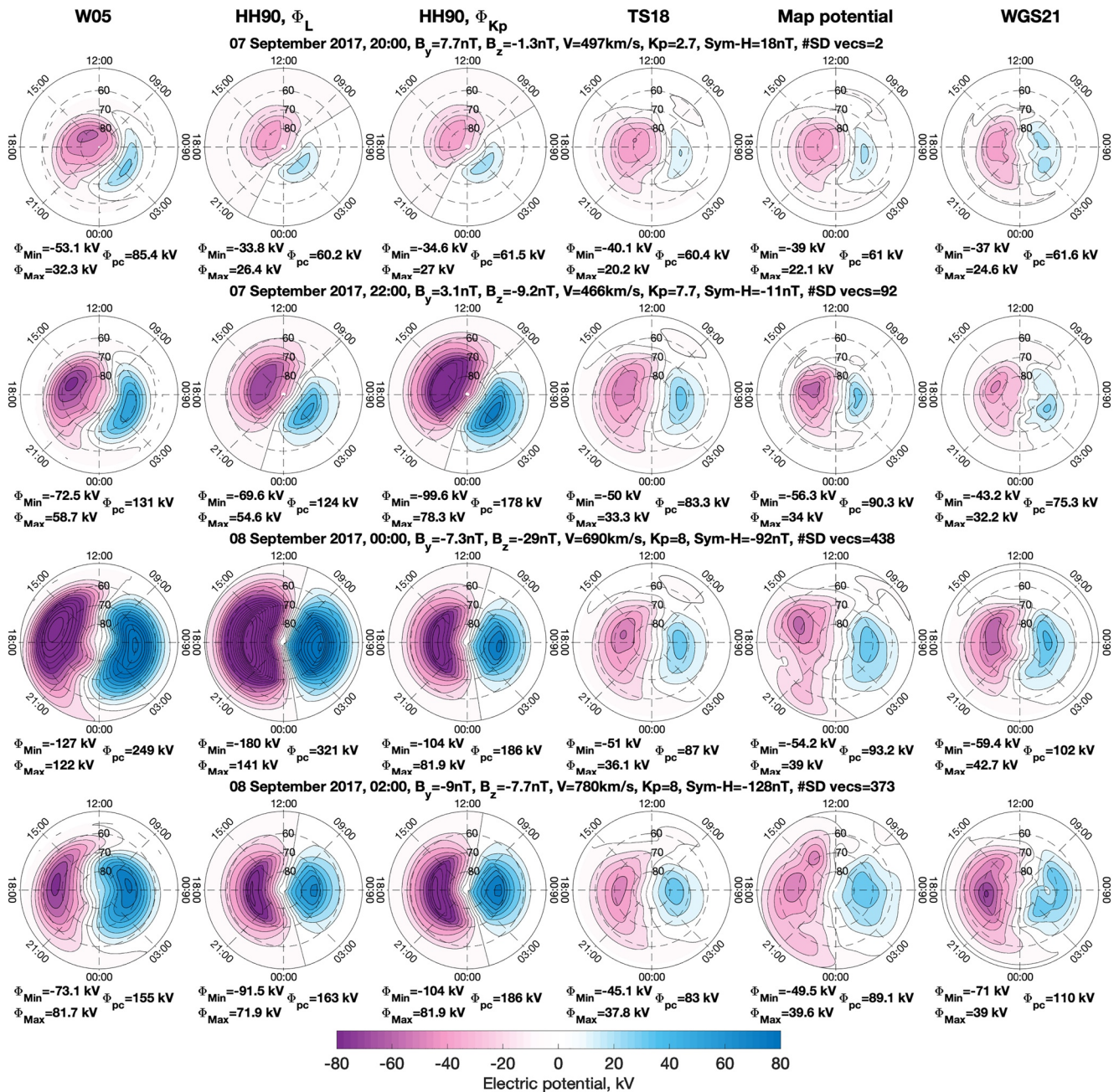


**Figure 3.** Convection maps in magnetic coordinates with contour lines representing 10 kV intervals for the models over four time intervals. Purple/pink represents negative electric potential and blue represents positive electric potential, as shown in the color bar. A selection of parameters including the time, interplanetary magnetic field conditions, SW velocity,  $K_p$ , Sym-H and the number of Super Dual Auroral Radar Network vectors are provided per panel. Text below each map shows the maximum and minimum potential on the left and  $\Phi_{PC}$  on the right.

is stronger than the dawn cell ( $\Phi_{\text{max}}$ ) for all models. Map Potential shows the highest asymmetry of any model toward the end of the main phase with  $\Phi_{\text{res}} = -64$  kV at 00:52 UT on the 8th. During the recovery phase the W05 model has  $\Phi_{\text{res}} > 0$ , meaning the dawn cell has a higher magnitude. This can be seen in Figure 3 at 02:00 UT where  $\Phi_{\text{min}} = -73.1$  and  $\Phi_{\text{max}} = 81.7$  kV.

Panel G shows the mean EF vector magnitude  $|\bar{E}F|$  of all vectors above  $60^\circ$  magnetic latitude (Equation 10). The method for calculating EFs from electric potential data is described in Section 2.4. Trends in the time series are largely similar to those seen in panel E for  $\Phi_{PC}$  but calculating a parameter from a range of latitudes and longitudes allows us to include the HH90 response in the comparison. HH90 ( $\Phi_L$ ) has a similar  $|\bar{E}F|$  to W05 until

23:15 UT on the 7 September, with both having  $|\vec{EF}| \sim 35$  mV/m. From 23:15 UT the HH90 ( $\Phi_L$ ) parameter increases sharply to maximize with  $|\vec{EF}| \sim 80$  mV/m, approximately 160% of the maximum value of the W05 model. HH90 ( $\Phi_{Kp}$ ) has  $|\vec{EF}| \sim 50$  mV/m from shortly after 21:00 UT on the 7th until after 03:00 UT on the 8th. This is higher than the rest of the models until 23:15 UT when the  $|\vec{EF}|$  of HH90 ( $\Phi_L$ ) exceeds it and W05 increases to have a similar value until 02:00 UT. The values from the SuperDARN-based models are again a lot smaller with maximum values of  $|\vec{EF}|$  between  $\sim 23$  and  $\sim 31$  mV/m. Again TS18 saturates at  $\sim 20:50$  UT whilst WGS21 and Map Potential gradually increase through the main phase.

Panel H is a simple proxy for the convection reversal boundary co-latitude which is approximated by assuming the location of the maximum and minimum potentials lie on a circle containing the polar cap (Equation 11). Again the TS18 model saturates at moderate IMF conditions with a convection reversal boundary co-latitude of  $\sim 16^\circ$ . HH90 and W05 show expansion on similar scales to WGS21 and Map Potential throughout the main phase, despite having a much larger  $\Phi_{PC}$ . HH90 briefly contracts between 00:35-00:51 UT following the increase of  $B_z$  from  $\sim -28$  to  $\sim -15$  nT. The Map Potential convection map has a smaller radius than the other models during the initial phase of the storm of  $9.5^\circ$ , before expanding to have the maximum radius of  $26^\circ$  at 00:40, 8th. The other models have average convection reversal boundary co-latitudes located between  $18^\circ$  and  $22^\circ$ .

In panel I we show the LLB for the SuperDARN-based models and W05 which we have chosen to be at the midnight boundary. An estimation of the HH90 LLB is included as described in Section 2.4. Here the models behave very differently. From 20:00–23:00 UT on the 7th, the W05, TS18 and HH90 ( $\Phi_L$ ) have a similar LLB, stabilizing at  $\sim 50^\circ$ . Shortly after 23:00 UT IMF  $B_z$  drops further causing W05, HH90 ( $\Phi_L$ ) and Map Potential to lower their boundaries to  $\sim 40^\circ$ . WGS21 has a HMB of  $\sim 60^\circ$  during the initial phase which drops down to  $50^\circ$  during the main phase and does not increase significantly during the first 130 min of the recovery phase. The TS18 HMB remains constant at  $51.5^\circ$  from 20:50 UT on the 7th to 02:00 UT on the 8th. Map potential and WGS21, the two models that are not defined using IMF and solar wind parameters (unless there are few SuperDARN vectors available for Map Potential), extend to lower latitudes much later than the other models. Both extend to  $\sim 50^\circ$  latitude for the start of the main phase whereas the TS18, HH90, and W05 models extend to  $\sim 50^\circ$  latitude at  $\sim 21:00$  UT.

### 3.2. Model Comparison of Snapshots of Convection Pattern

Figure 3 shows four snapshots of the convection from each of the models, from left to right: W05, HH90 ( $\Phi_L$ ) (taking  $\Phi_L$  as the  $\Phi_{PC}$  input), HH90 ( $\Phi_{Kp}$ ), TS18, Map Potential and WGS21. From top to bottom the snapshots span 20:00 UT on 7 September to 02:00 UT on 8 September, in two hour intervals. The snapshot times line up with vertical blue lines from the time series shown in Figure 2 and are chosen to show a range of conditions through the initial, main and recovery phases of the storm. The individual plots show northern hemisphere convection maps in AACGM-v2 coordinates with contour lines drawn at 10 kV intervals. Purple/pink represents negative electric potential and blue represents positive electric potential, as shown in the color bar. A selection of metadata including the time, IMF conditions ( $B_Y$  and  $B_Z$ ), SW velocity,  $V$ ,  $K_p$ , Sym-H and the number of SuperDARN vectors (#SD vecs) are presented above each row.

The first snapshot is during the initial phase when  $B_y = 7.7$  nT and  $B_z = -1.3$  nT. The convection map produced by W05 descends to  $\sim 58^\circ$  latitude in the nightside (around midnight) and has a maximum and minimum electric potential at 3 and 15 hr MLT respectively. The dusk cell (pink) is centered around  $80^\circ$  latitude, enveloping the magnetic pole, whilst the dawn cell is lower in latitude centered around  $70^\circ$ . The two versions of HH90 give similar patterns with low magnitude electric potential with the convection patterns confined to above  $\sim 67^\circ$  latitude on the nightside. Due to the relatively high positive  $B_y$  the zero potential lines are rotated 2 hr clockwise of the midnight line and 4 hr clockwise of the noon line. The TS18 convection pattern has a similar shape to W05 but TS18 has  $\sim 70\%$  the magnitude of  $\Phi_{PC}$  from W05. The convection pattern appears to be rotated  $\sim 3$  hr anti-clockwise compared to W05. The Map Potential model in this instance has only 2 SuperDARN vectors available and so is almost exclusively determined by the TS18 model. WGS21, parameterized only by storm phase, shows a convection pattern for late in the initial phase. The convection pattern resembles TS18/Map Potential patterns with cells roughly symmetrical about the dawn-dusk meridian.

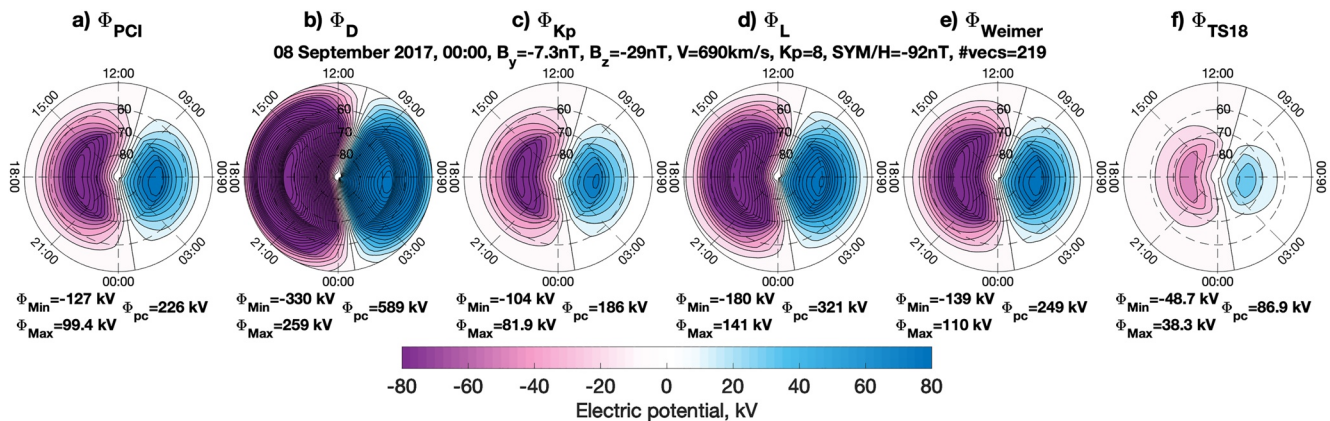


**Figure 4.** Convection maps in magnetic coordinates with contour lines representing 10 kV intervals for the Heelis model with six  $\Phi_{PC}$  proxies over four time intervals. Purple/pink represents negative electric potential and blue represents positive electric potential, as shown in the color bar. A selection of parameters including the time, interplanetary magnetic field conditions, SW velocity, Polar Cap Index, Sym/H and the number of Super Dual Auroral Radar Network vectors are provided per panel.

By 22:00 UT the W05 pattern has expanded to lower latitudes, rotated anti-clockwise and  $\Phi_{PC}$  has increased to 131 kV. HH90 ( $\Phi_L$ ) has maximum and minimum potentials with similar locations and magnitudes to W05, but the location of the dayside and nightside “throats” is different; note that HH90 defines the zero potential line at  $\sim 9$  and  $\sim 23$  hr MLT owing to the way the model is parameterized. The locations of these zero potential lines are dependent on  $B_y$  and do not allow the positive and negative cells to occupy the same local time, in contrast to W05 in the midnight local time sector. HH90 ( $\Phi_{Kp}$ ) has a higher magnitude  $\Phi_{PC}$  and as such the convection expands equatorward by a further  $\sim 2^\circ$  compared to that with the  $\Phi_L$  input. TS18 is a similar shape to W05 but with much lower  $\Phi_{PC}$  of 83.3 kV. Compared to HH90 it is rotated anti-clockwise by several hours, and the nightside throat is rotated anti-clockwise by  $\sim 1$ – $2$  hr compared to W05. Map Potential now has 92 vectors contributing to the fit and so shows a different picture to TS18 and is constrained to higher latitudes. WGS21 resembles TS18 with less uniformity and less asymmetry between the dawn and dusk cells.

By 00:00 UT  $B_z$  has reached  $-29$  nT with a SW velocity of 690 km/s, which results in very high electric potential magnitudes. W05 has expanded such that the lower latitude boundary is now located below  $50^\circ$  latitude. The polar cap boundary as inferred from the latitude of the cell foci has expanded in comparison to the map at 20:00 UT. HH90 ( $\Phi_L$ ) has an even higher  $\Phi_{PC}$  and greater asymmetry between the maximum and minimum potentials. Negative IMF  $B_y$  results in an anti-clockwise rotation of  $\sim 2$  hr of MLT compared to the previous time interval. HH90 ( $\Phi_{Kp}$ ) has the same input  $\Phi_{PC}$  as at the previous time point, resulting in a similar convection pattern with any differences attributed to the rotation of the convection pattern by 2 hr of MLT due to the decrease of  $B_y$ . TS18 has not changed significantly from 22:00 UT because the model has reached its maximum  $E_{sw}$  bin. Map Potential extends to lower latitudes and has slightly higher potentials than TS18 but much lower potentials than the W05 and HH90 patterns. WGS21 is now in the main phase of the storm and reaches a higher  $\Phi_{PC}$  than the other SuperDARN models but still much lower than the W05 and HH90 models.

The main phase of the storm ends at 01:08 UT, and so the final snapshot at 02:00 UT is during the recovery phase of the storm. W05 relies on delayed values of IMF and SW conditions and therefore shows a contracted polar cap with a much lower  $\Phi_{PC}$  than the previous snapshot. W05 at 02:00 UT is the only map from our chosen snapshots that has a higher magnitude dawn cell than dusk cell as  $|\Phi_{max}|$  is higher than  $|\Phi_{min}|$ . HH90 ( $\Phi_L$ ) likewise uses IMF and SW values so has contracted to higher latitudes. HH90 ( $\Phi_{Kp}$ ) has increased very slightly in magnitude due to Kp increasing from 7.7 to 8. Otherwise the pattern remains the same as above with a further anti-clockwise rotation due to a further decrease in  $B_y$ . TS18 is still much the same, as the climatology still corresponds to its highest  $E_{sw}$  bin. Map Potential, using SuperDARN measurements from the interval, shows the convection map still extends to lower latitudes (below  $50^\circ$  latitude) and still has a similar  $\Phi_{PC}$  ( $\Phi_{PC} \sim 89.1$  kV) than the value during the main phase of the storm. WGS21 is now in the recovery phase and mainly shows an increased magnitude of the dusk cell from  $-59.4$  to  $-71$  kV.

Figure 4 highlights how big an effect the choice of the  $\Phi_{PC}$  proxy has on the convection map output by HH90. We show six examples, all for the same time point of 00:00, 8 September. From a) to f) we take the input of  $\Phi_{PC}$

to be  $\Phi_{PC}$  (Equation 4),  $\Phi_D$  (Equation 7),  $\Phi_{Kp}$  (Equation 2),  $\Phi_L$  (Equation 1), followed by the  $\Phi_{PC}$  output by the W05 and TS18 models at the same time point. The rotation of the pattern remains the same for each as it is a function of  $B_y$  which remains the same. However the magnitude of the electric potential and the extent to which the pattern expands is very different. Panel f) takes the input of  $\Phi_{PC}$  to be that which is output from the TS18 model. As TS18 had saturated by this time point,  $\Phi_{pc} = 86.9$  kV is much lower than the other estimates of  $\Phi_{PC}$  and results in the pattern being confined to above  $\sim 62^\circ$  latitude. At the other end of the extremes is panel b) which takes the dayside reconnection rate,  $\Phi_D$  as input. This results in  $\Phi_{pc} = 589$  kV,  $6.8\times$  higher than the corresponding value from panel f). The remaining maps range from  $\Phi_{PC} = 186$  kV using  $\Phi_{Kp}$  (c) and a  $\Phi_{PC} = 321$  kV using  $\Phi_L$  (d). The lower boundary of the pattern extends from  $\sim 58^\circ$  to  $\sim 50^\circ$  with the increase in magnitude from c) to d). As it is the Kp equation in c) that is currently used within AENeAS we will continue to compare  $\Phi_{Kp}$  input throughout our analysis. We will additionally use  $\Phi_L$  as input to HH90 as a comparison because it is the optimum coupling-function according to Lockwood and McWilliams (2021), and it has a less extreme response to the low  $B_z$  values seen within the September 2017 storm.

### 3.3. Electric Field Vectors for MLT Bands

In this section we look in more detail at the variation of the north-south EF component throughout the storm by taking latitudinal slices across the dawn-dusk line (6–18 MLT) and the noon-midnight line (12–24 MLT). The EF vectors were calculated from the gradient of the potential using the method specified in Section 2.4. We have converted the north-south EF vector into Cartesian coordinates such that, along the dawn-dusk line, positive EF is dawn-to-dusk directed (as shown in the left column of Figure 5) and along the midnight-noon line positive EF is midnight-to-noon directed (as shown in the right column of Figure 5). By looking at the MLT bands at dawn (MLT = 6) to dusk (MLT = 18), and noon (MLT = 12) to midnight (MLT = 24), we see how the topology of the polar cap and lower latitude EF patterns change throughout the storm, as well as the differences in EF magnitude between the different models.

In panel A we have plotted the IMF  $B_y$  and  $B_z$  components of the field for easy comparison with the EF color plots. The left column plots the dawn-to-dusk directed component of the EF according to the color bar. The  $x$ -axis shows the time and the  $y$ -axis plots latitude where it increases from  $50^\circ$  to  $90^\circ$  latitude along the MLT = 6 line, where it crosses the pole and decreases from  $90^\circ$  to  $50^\circ$  along the MLT = 18 line. The right column plots the midnight-to-noon directed component of the EF along the MLT = 12 to MLT = 24 line. The models are each plotted as rows with B) WGS21, C) TS18, D) Map Potential, E) HH90 ( $\Phi_L$ ), F) HH90 ( $\Phi_{Kp}$ ) and G) W05 from top to bottom. Colors represent the EF strength and direction as shown by the color bar. Gray shows where there is no data, either because it is below the LLB, or it is close to the magnetic pole.

Beginning with the left hand column, we see a dawn-to-dusk directed EF (positive) within the polar cap (corresponding to anti-sunward flow) and a dusk-to-dawn directed EF (negative) at auroral latitudes (corresponding to sunward flow). This pattern is consistent across the entire storm with equatorward expansion of the polar cap and the lower latitude boundary evident throughout the storm. Panels E–G, that is, HH90 ( $\Phi_L$ ), HH90 ( $\Phi_{Kp}$ ), and W05, have higher EF vector magnitudes than the SuperDARN-based models in panels B–D, throughout the storm. WGS21 (Panel B) shows significant variation, particularly in its dawn-to-dusk directed EF within the polar cap and shows more fine structure compared to the other models. TS18 (Panel C) saturates at  $\sim 20:50$  UT, as previously seen, and shows a similar pattern from then until 02:00 UT. Map potential (Panel D) shows a sharp change at  $\sim 21:06$  UT when the model switches from relying heavily on the TS18 climatologies to using available SuperDARN data. Map Potential initially has a relatively strong EF magnitude, both within the pole and at auroral latitudes, but this weakens during the main phase of the storm as the pattern extends to lower latitudes. At auroral latitudes HH90, with both  $\Phi_L$  and  $\Phi_{Kp}$  (Panels E–F) has a two-band structure for the dusk-to-dawn directed vectors, with one band centered at around  $\sim 70^\circ$  and a thinner band at  $\sim 60^\circ$  throughout. HH90 has exponentially decreasing potential outside of the polar cap so no LLB (low latitude gray zone) is shown; the EF magnitude tends toward zero. For all models the overall pattern is reflected across the pole but there are some asymmetries between dusk and dawn. Each of the models has stronger dawn-to-dusk directed EF within the polar cap on the dawn side compared to the dusk side during the initial phase. For WGS21, TS18, Map Potential and W05 (Panels B–D and G) this pattern continues throughout the main phase of the storm but the HH90 models (Panels E–F) flip to having stronger dusk side EF magnitude within the polar cap when IMF  $B_y$  is sufficiently negative for example, at  $\sim 23:38$ – $00:32$  UT and  $\sim 00:56$ – $03:18$  UT corresponding to when the IMF  $B_y$  component

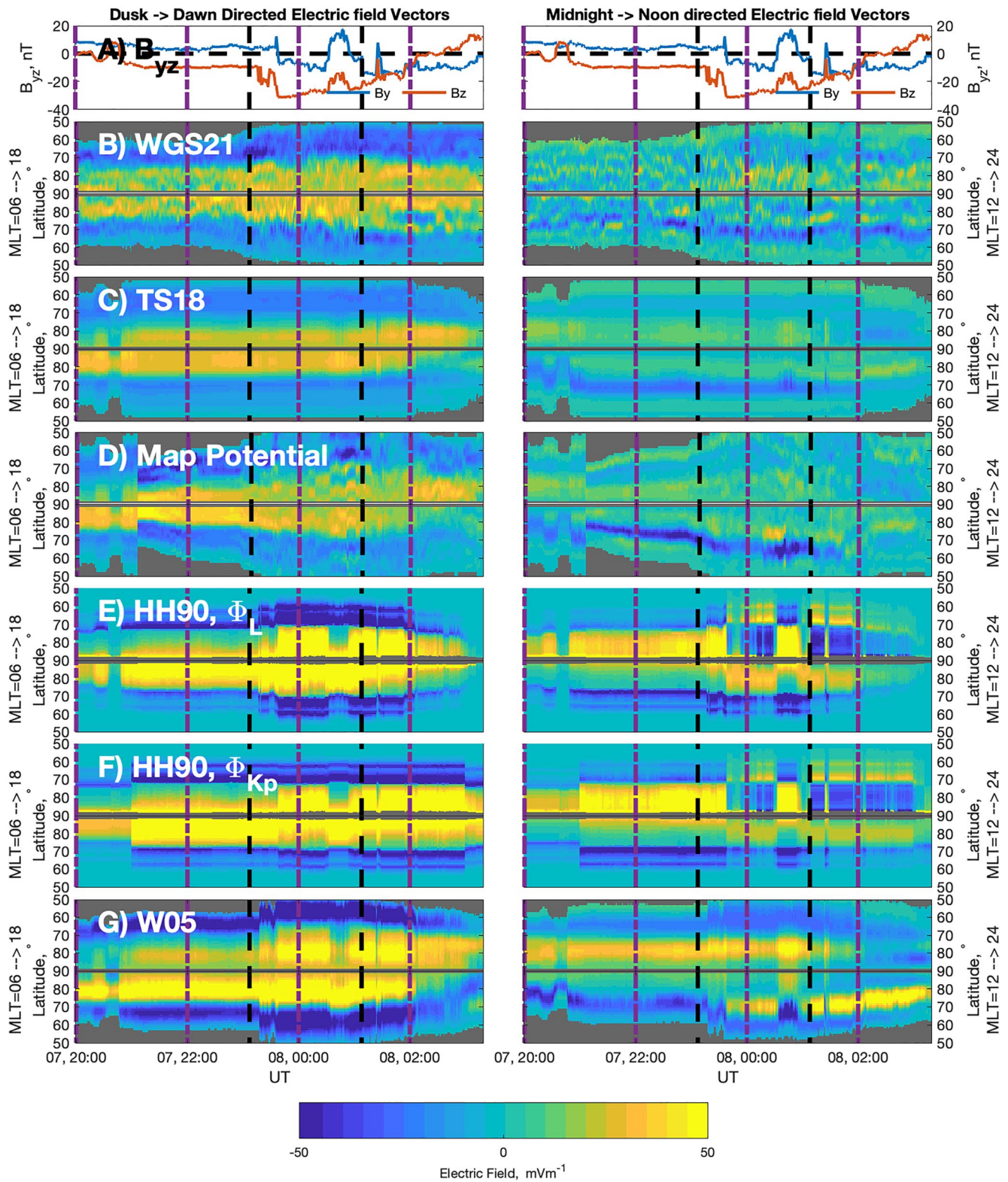


**Figure 5.** Electric field vectors with the dawn-dusk line with dawn-to-dusk direction and the right column is along the midnight-noon line with midnight-to-noon direction are shown on the left and right column, respectively. Panel A has interplanetary magnetic field  $B_y$  and  $B_z$  for reference. Vertical dashed black lines represent the start and end of the main phase. Vertical dashed purple lines match the snapshots from Figure 3.

switches from positive to negative. W05 shows enhancements in the dusk-side dawn-to-dusk directed field at the same times. WGS21 (Panel B) shows an enhancing dusk-to-dawn directed region of EF (dark blue) shortly after the 22:00 UT in the dusk-side auroral zone.

The right hand column is along the  $MLT = 12$  to  $24$  line, we generally see a midnight-to-noon directed EF (positive) within the polar cap and a noon-to-midnight directed EF (negative) at auroral latitudes but the patterns are less consistent than they were along the dawn-dusk line. WGS21 (Panel B) shows more variability with instances of positive and negative vectors scattered around a consistent noon-to-midnight directed strip (blue) of EF between  $65^\circ$  and  $75^\circ$  latitude at noon. TS18 (Panel C) shows weak EF magnitude, particularly below  $65^\circ$ , with the strongest EF being noon-to-midnight directed at auroral latitudes on the noon-side. Likewise Map Potential (Panel D) has relatively weak EF vector magnitude with the strongest vectors being noon-to-midnight directed on the noon-side from  $\sim 21:00$  UT, which then expands from  $\sim 80^\circ$  latitude to  $\sim 60^\circ$  by  $\sim 00:30$  UT on the 8th. The noon-side HH90 models, with both  $\Phi_L$  and  $\Phi_{kp}$  (Panels E–F) show a weaker but similar pattern to  $MLT = 18$ . However at midnight HH90 very clearly shows where the zero potential line is switching from pre to post midnight due to changes in IMF  $B_y$ . If  $B_y = 0$  the zero potential line is located at 23.5 hr MLT, with negative  $B_y$  rotating it clockwise, and positive  $B_y$  rotating it anti-clockwise, by 0.15 hr per nT. When  $B_y = 0.3$  nT the direction of the EF bands switch. A plot showing this can be seen in Figure S5 in Supporting Information S1. W05 (Panel G) has a midnight-to-noon directed EF near the polar cap on the nightside but only very weak EF within the pole on the dayside throughout, except for during the period of positive  $B_y$  around  $\sim 00:30$  UT when it strengthens. When IMF  $B_z$  drops to less than  $-30$  nT at  $\sim 23:30$  UT there is a strong midnight-to-noon directed EF around  $70^\circ$  latitude at noon, forming a clockwise spiral of equatorward-directed EF from the high latitude negative EF at  $MLT = 18$ , through noon at  $70^\circ$ , through  $MLT = 6$  around  $60^\circ$  and to midnight. This spiral is briefly interrupted at  $MLT = 12$  around  $\sim 00:30$  UT by the switch to positive  $B_y$  but reappears around 01:00 UT when  $B_y$  returns to negative. See Figures S2 and S3 in Supporting Information S1 for an example of the global EF for snapshots at the times of the vertical dashed purple lines.

### 3.4. Direct Comparison of Models

In Figures 6 and 7 the times included are from 11:02 UT, 7 September, the start of the initial phase, until 23:59 UT, 8 September, during the recovery phase. This is a much wider time range than considered up until now that encompasses all of the initial and main phases of the storm and the first third of the recovery phase (23 of 66 hr). For Figure 6 the upper half of the matrix has scatter plots plotting the transpolar voltage,  $\Phi_{PC}$ , from model A against that of model B at time  $t$ . The  $x = y$  line is included to show where the points would lay if the model output was the same. If the points are above the  $x = y$  line the model on the  $y$ -axis has a larger  $\Phi_{PC}$  than the model on the  $x$ -axis at that time.

On the bottom half of the matrix we show histograms of  $\Phi_{PC}$  from model A minus  $\Phi_{PC}$  from model B. The black line marks zero difference and is equivalent to  $x = y$ , that is, if the two models were the same the distribution would be a delta function at zero. The mean difference in the models  $\Phi_{PC}$  is overplotted with a dashed purple line with the standard deviation represented as a horizontal error bar about the mean.

The panels are organized as a grid such that the first row is map potential on the  $y$ -axis versus each of the models on the  $x$ -axis in each column. The first column shows the histograms of map potential minus each of the models. Each row is labeled by the first model (A–F) and each column is labeled by the second model (A–F) such that AB) is the scatter plot of TS18 versus Map Potential (MP) and the corresponding histogram BA is Map Potential minus TS18. The colors represent the phase of the storm. The histograms are stacked vertically such that the top (blue) represents the initial phase, the middle (orange) the main phase and the bottom (yellow) the recovery phase. The histograms are not overlapping that is, the main phase has the lowest counts as it contains the fewest time points.

Panel AB) shows that there is a clear saturation in TS18 at  $\sim 90$  kV, with the main phase of the storm varying from  $\sim 80$ – $120$  kV for Map potential but  $\Phi_{PC}$  from TS18 only from  $\sim 85$ – $91$  kV. BA shows TS18 and Map potential are the most similar, with the histogram centered around zero with a slight bias toward Map potential having stronger  $\Phi_{PC}$  than TS18 (mean difference of 2.3 kV). AC)–AE) show that Map potential saturates compared to HH90 and W05. All models but TS18 tend to have stronger  $\Phi_{PC}$  than Map Potential for the same time point. This is demonstrated by the points being below the  $x = y$  line in row A. Similarly, the histograms of Map potential in column A

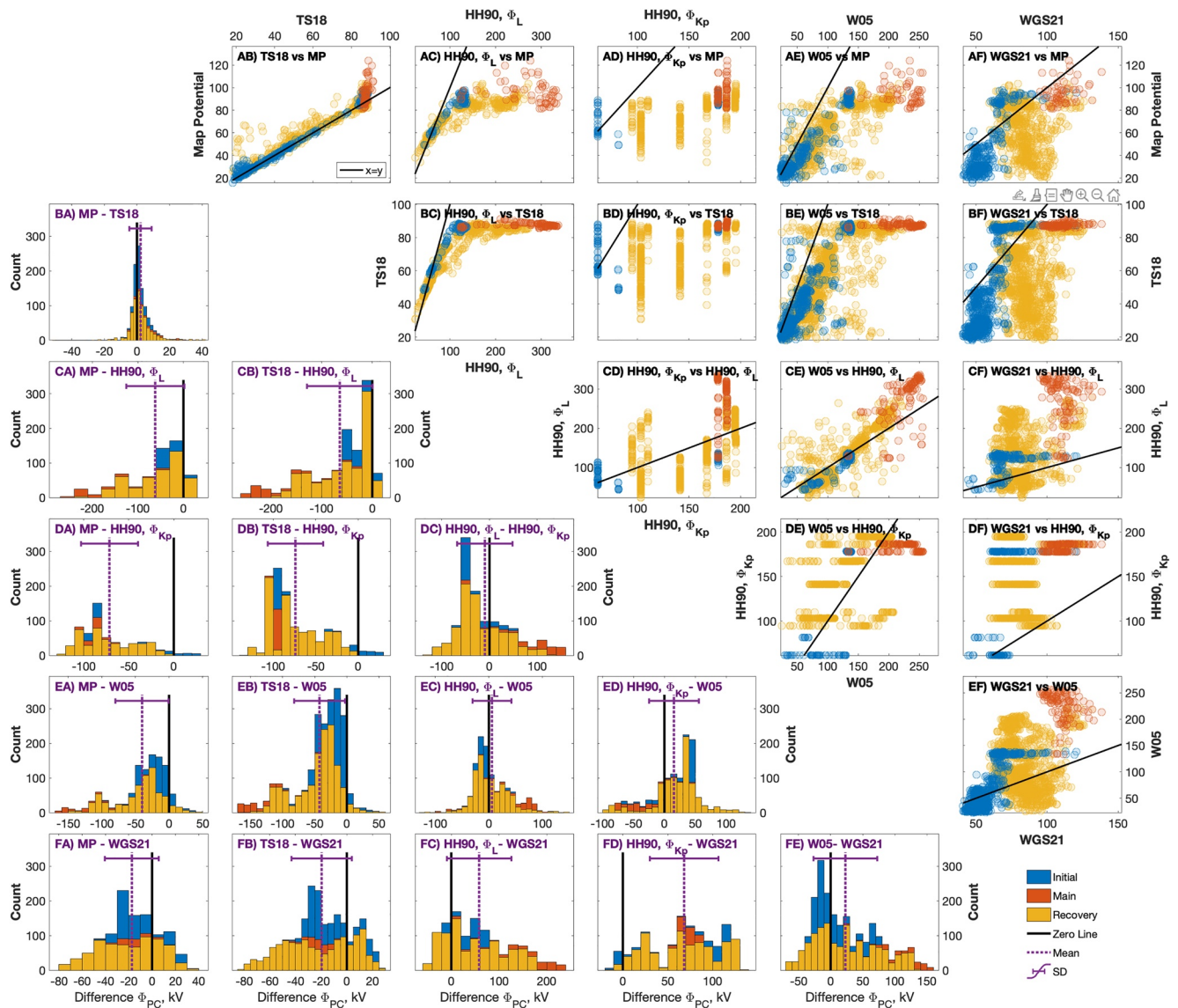


**Figure 6.** (Right side) scatter plots of  $\Phi_{PC}$ , kV from model A against that of model B at time  $t$ .  $x = y$  line is in black. (Left side) Histogram of  $\Phi_{PC}$ , kV from model A minus that of model B at time  $t$ . The colors represent the phase of the storm at time  $t$ . The histograms are stacked such that the top (blue) represents the initial phase, the middle (orange) represents the main phase and the bottom (yellow) represents the recovery phase. The zero difference line is in black. The mean in dashed purple with the standard deviation represented by a horizontal error bar.

are biased toward negative values as all models but TS18 have generally higher  $\Phi_{PC}$ , especially during the main phase, and negative mean differences. The row B scatter plots again shows a clear saturation of  $\sim 90$  kV from the TS18 model ( $y$ -axis). In BC) HH90 ( $\Phi_L$ ) is relatively similar to TS18 until this saturation point. In column B each histogram is shifted toward negative values and has a negative mean difference showing that  $\Phi_{PC}$  for TS18 is smaller than each of the other models. In CE) HH90 ( $\Phi_L$ ) and W05 show high correlation with  $\Phi_L$  generally having slightly higher  $\Phi_{PC}$  than W05. The corresponding histogram EC) is almost centered around zero (mean difference of 5.6 kV) but with a standard deviation of 36 kV. During the main phase  $\Phi_L$  can be  $\sim 50$ – $80$  kV higher than that of W05.  $\Phi_L$  shows the highest variability compared to the other models with differences between  $\Phi_L$  and all models but W05 having a standard deviation of 58–68 kV. The scatter plots in column/row D show that the  $\Phi_{Kp}$  proxy (Equation 2) is ordered in discrete steps and it consequently does not have much correlation with the other models. In column F, WGS21 shows a spread in all cases. Toward the end of the initial phase (in blue;  $\sim 20:50$  UT to beginning of main phase) WGS21 gradually increases from  $\sim 60$ – $120$  kV whilst each of the other models remains constant (as was seen in Figure 2).

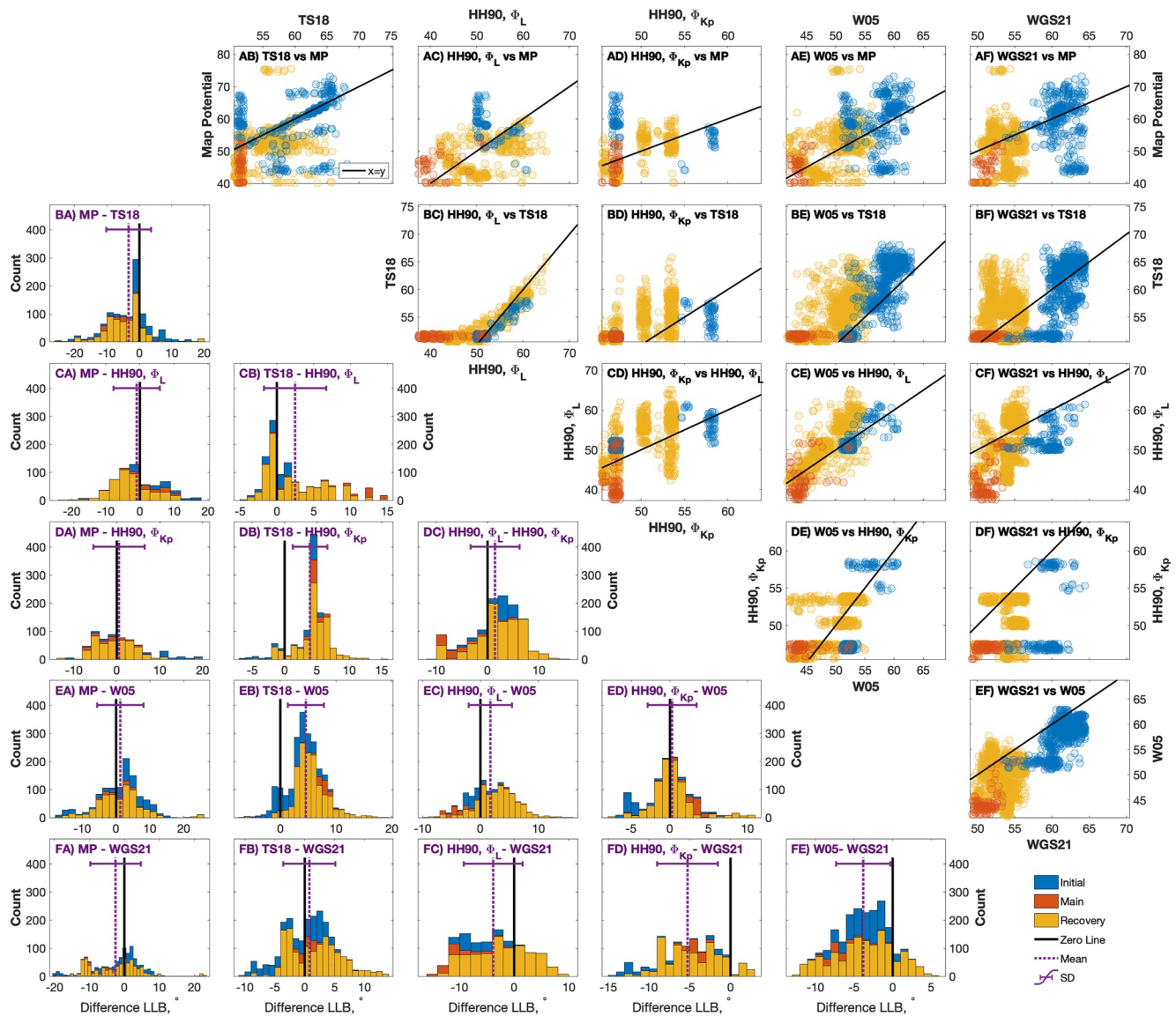


**Figure 7.** (Right side) scatter plots of the lower latitude boundary from model A against that of model B at time  $t$ .  $x = y$  line is in black. (Left side) Histogram of lower latitude boundary from model A minus that of model B at time  $t$ . The colors represent the phase of the storm at time  $t$ . The histograms are stacked such that the top (blue) represents the initial phase, the middle (orange) represents the main phase and the bottom (yellow) represents the recovery phase. The zero difference line is in black. The mean in dashed purple with the standard deviation represented by a horizontal error bar.

Figure 7 is of the same form as Figure 6 but shows a comparison of the LLB/HMB for the models. As for Figure 2, the LLB is the HMB for the SuperDARN-based models and the LLB at the midnight boundary for W05. An estimation of the HH90 LLB is included as described in Section 2.4. The convection maps from all but the HH90 models are calculated at  $1^\circ$  discrete steps and hence a randomized value between  $\pm 0.5^\circ$  is added to the LLB to aid the visualization of the density of discrete data. Without this the discrete points are likely to be overplotted, making it difficult to distinguish between low and high density data occurrence. The magnetic latitude of HH90 is calculated as described in Section S1.2 in Supporting Information S1.

In Figure 6 we saw high correlation between  $\Phi_{PC}$  of TS18 and Map Potential. In Figure 7 we see little correlation between the LLB of TS18 and Map potential in panel AB). Map potential generally has a lower boundary than TS18 as indicated by most of the points being below the  $x = y$  line, and the negative shifted histogram in BA) which has a mean of  $-3.3^\circ$ . Column/row a shows Map potential and the other models have little correlation and a lot of scatter. BC) shows high correlation between HH90 ( $\Phi_L$ ) and TS18, until the TS18 LLB saturates at  $51^\circ$

(corresponding to the previous saturation seen in electric potential during the main phase of the storm). W05 and WGS21 in columns E and F show the LLB at distinct latitude bands in the initial, main and recovery phases. For WGS21 (column F) the initial phase has a LLB centered around 60–65°, main ~50° and recovery ~52–57°. For Weimer (column E) the initial phase has a LLB centered between 50–63°, main ~42–45° and recovery ~42–57°. During the initial phase the WGS21 LLB changes from 50–60° whilst TS18, HH90 ( $\Phi_L$ ), HH90 ( $\Phi_{Kp}$ ), and W05 have a constant lower boundary; this is shown by the horizontal line of blue markers in column F. The majority of the histograms are centered around the zero line, with much less shift toward the positive/negative than was seen in Figure 6. Standard deviations range between 2.7° in (DB) and 7.2° in (FA). Exceptions include TS18 compared to HH90 ( $\Phi_{Kp}$ ) (DB) and to W05 (EB) which are shifted to the positive that is, they have a significantly lower LLB than TS18, as well as HH90 ( $\Phi_{Kp}$ ) compared to WGS21 (FD) which has a mean of  $-5.3^\circ$ .

#### 4. Discussion

The aim of this study was to compare the output of modern high-latitude ionospheric EF models, based on SuperDARN measurements, to older models based on spacecraft data. EF models represent an important component of thermospheric models due to their influence on Joule heating (Bruinsma et al., 2021). It is possible that incorporating the more modern models into large atmosphere models such as AENeAS will improve their forecasting ability. We have compared the versions of the Heelis model (HH90) (M. Hairston & Heelis, 1990; HAO, 2018; Heelis et al., 1982), and the Weimer model (W05) (Weimer, 2005b) that are both implemented in AENeAS with the Thomas and Shepherd (TS18) (Thomas & Shepherd, 2018) and Walach and Grocott (WGS21) (Walach et al., 2021) models, as well as the SuperDARN Map Potential (Ruohoniemi & Baker, 1998), during the September 2017 geomagnetic storm. During geomagnetic storms, Joule heating is significantly enhanced. Hence, it is important to be able to forecast well for storm time conditions. In this section we highlight the differences in the EF contribution to Joule heating that arise from the different models during storm times and the possible reasons for the differences.

Although we are only studying a single storm it encompasses a wide range of solar wind and IMF conditions to highlight differences in both the model topologies and magnitudes. The W05, HH90 ( $\Phi_L$ ) and TS18 models are calculated using 1-min cadence solar wind and IMF data as input, and as such are directly sensitive to the variability in these parameters. HH90 ( $\Phi_{Kp}$ ) is dependent on the 3-hourly Kp index as well as 1-min cadence IMF  $B_y$ . WGS21 is parameterized by storm phase and so is not directly sensitive to variations in the solar wind drivers but is designed to better capture the time history of the magnetospheric response. As a forecast model, however, WGS21 is limited by the need to await the start and end of each storm phase. Map Potential uses SuperDARN measurements of the event, so it is not suitable for forecasting either but can act as a baseline, with the caveat that two of the other models we are comparing it to are also based on SuperDARN data.

The variations in the magnitudes of the electric potential outputs across the observed range of conditions highlight some of the main differences between the models. Under quiet and moderate conditions the models display relatively similar outputs. This is particularly clear during the initial and recovery phases in Figure 6. Hence, we would expect estimates of Joule heating to be relatively consistent between models at these times. However, when IMF  $B_z$  drops toward  $-30$  nT, the spacecraft-based models (W05 and HH90) can have more than double the transpolar voltage of the SuperDARN-based models. Haaland et al. (2007) likewise found W05 to have double the transpolar voltage to the SuperDARN-based model RG05 (Ruohoniemi & Greenwald, 2005) during negative  $B_z$ . This would relate to a difference in Joule heating estimates of more than a factor of 4.

For the TS18 model the primary reason for the underestimation with respect to the spacecraft-based models is simple. When  $B_z < -10$  nT in Figure 2,  $\Phi_{PC}$ ,  $r_{pc}$ , and HMB in TS18 all saturate at  $\sim 90$  kV,  $15^\circ$ , and  $51^\circ$ , respectively. This is because  $E_{sw} > 3$  mV/m,  $110 < \theta_{clk} < 250^\circ$ , and dipole tilt is neutral during this time. In this range, there are only three potential patterns available in the TS18 model which all have quite similar  $r_{pc}$  and HMB and  $\Phi_{PC}$  only varies between 84 and 91 kV (see Figure 6 and Table 2 of Thomas and Shepherd (2018)). The data used in TS18 was collected during solar cycle 24, which was a much less active solar cycle than solar cycle 21, when the data used in W05 was collected (see Figure 1). Thomas and Shepherd (2018) lowered their solar wind EF magnitude,  $E_{sw}$  bins to account for the smaller measurements compared to previous SuperDARN models (Cousins & Shepherd, 2010; Pettigrew et al., 2010; Ruohoniemi & Greenwald, 1996). This restriction suggests that this model is not wholly suitable for describing variations in convection during extreme storm times. This is unsurprising given the model is designed as a background model for the Map Potential. Thomas and Shepherd (2018) have a Kp counterpart

statistical characterization of ionospheric convection which is parameterized by Kp and IMF clock angle. The highest Kp bin (<8) shows a  $-B_z$  convection pattern that extends to lower latitudes on the nightside and has higher magnitude electric potential than the highest  $E_{sw}$  bin ( $3.0 \leq E_{sw} < 20.0$  mV/m (Thomas & Shepherd, 2018)). The maximum value of  $\Phi_{PC}$  using the Kp version of TS18 is  $\sim 97$  kV which is still below the maximum values of  $\Phi_{PC}$  found using each of the other models during this September 2017 event.

For Map Potential the  $E_{sw}$  constraint is partly removed because of the addition of SuperDARN measurements from the September 2017 storm itself.  $r_{pc}$  and HMB expand equatorward to latitudes comparable to W05 and HH90 ( $\Phi_L$ ) but  $\Phi_{PC}$  for Map Potential increases to  $< \sim 120$  kV (30% increase) compared to  $> \sim 200$  kV for W05 and HH90 ( $\Phi_L$ ). This suggests that either the large-scale  $\Phi_{PC}$  measure is still heavily constrained by the TS18 model and/or other factors are at play. First, SuperDARN has been known to underestimate the  $\Phi_{PC}$  when the polar cap expands beyond the field of view of the radars (S. Shepherd et al., 2002). Since this study, the SuperDARN network has expanded to both higher and lower latitudes. However, Thomas and Shepherd (2018) acknowledge that during extreme events  $\Phi_{PC}$  is likely to be underestimated due to the convection pattern expanding equatorwards of the mid-latitude radars. This may be the case for the extreme storm time variations considered here as the HMB saturates at  $40^\circ$ , which is an artificial limit in the model due to the lowest available latitude of radar measurement. Second, it has also been noted that when compared to DSMP ion drifts, SuperDARN velocities have been shown to be smaller (Drayton et al., 2005). Doppler velocities measured by SuperDARN are progressively under-estimated with decreasing ionospheric refractive index caused by increasing electron density (Gillies et al., 2009), which may be expected due to enhanced auroral particle precipitation during higher  $\Phi_{PC}$  and corresponding geomagnetic activity.

For WGS21, although it is not constrained by TS18, it is based on SuperDARN data and so could be underestimating  $\Phi_{PC}$  during extreme events due to the refractive index and the pattern extending beyond the equatorward extent of the radars; indeed the WGS21 HMB saturates close to  $50^\circ$ , like TS18. Alternatively, or additionally, WGS21 is calculated from 54 storms during solar cycle 24, the same time period as TS18, of which only two storms (26 September 2011 and 22 June 2015) have a more negative  $B_z$  than that seen in the 7–8 September 2017 storm. Likewise, only two (9 March 2012 and 22 June 2015) have Kp higher than or equal to that seen in the 7 September 2017 storm, meaning this storm is toward the more extreme end of the events used within WGS21. This could suggest that WGS21 is biased to underestimate  $\Phi_{PC}$  during more extreme storms than the average storm of solar cycle 24. However, one feature of WGS21 is that it does provide a forecast of the temporal variability introduced to the convection EF during a storm by the inclusion of time history. The delayed solar wind values used as input for W05, HH90, and TS18 may result in over or under estimations of the magnitude of  $\Phi_{PC}$  as these models take no account of how long the  $B_z$  component has been negative, which is an indication of how much energy has been added to the system through reconnection.

In contrast to the TS18 and WGS21 models whose solutions are binned averages that are constrained to the ranges of the data used in their development, there is no such restriction in the HH90 and W05 models. By construction, the ionospheric electric potential solution in these models is described by parameters that are continuous functions of the input control variables, allowing the solutions to be extrapolated even beyond the range of the underlying observations. However the choice of parameter functions differs within the HH90 model and between it and the W05 model. For HH90 the strong potentials seen during the main phase of the storm are a result of the input parameter  $\Phi_{PC}$ ; the maximum potential in the dawn cell is always 44% of  $\Phi_{PC}$  and minimum potential in the dusk cell is always  $-56\%$  of  $\Phi_{PC}$ . Maps showing the effect of the choice of  $\Phi_{PC}$  proxy are included in Figure 4, clearly showing how the choice of this input parameter affects the size and magnitude of the convection pattern.

The  $\Phi_{PC}$  output from the W05 model is most similar to the Lockwood parameter  $\Phi_L$ , which we used in HH90 but the W05 model does contain a saturation curve that levels to a gradual slope at higher magnitudes of the solar wind EF (Weimer, 2005a) (Equation 3 in Weimer (2005a)). There have been many observational, theoretical, and modeling studies for example, (M. R. Hairston et al., 2005; S. G. Shepherd, 2007; Kubota et al., 2017), that have found saturation of  $\Phi_{PC}$  for large  $E_{sw}$ . S. G. Shepherd (2007) suggests  $\Phi_{PC}$  saturates at  $< 300$  kV whilst Lockwood and McWilliams (2021) suggests a typical value between 150–200 kV. Figure S7 in Supporting Information S1 plots  $E_{sw}$  versus  $\Phi_{PC}$  which shows the saturation of W05 at  $\sim 250$  kV to be much higher than the artificial saturation of the SuperDARN based models and  $\Phi_{Kp}$ .  $\Phi_L$  shows a curved relationship with  $E_{sw}$  similar to W05 for lower values but it does not saturate.

The polar cap radius proxy,  $r_{pc}$  and the lower latitude boundary (or HMB) variations show both boundaries moving equatorward throughout the main phase of the storm as the  $\Phi_{PC}$  increases. The HH90 ( $\Phi_L$ ) and HH90 ( $\Phi_{Kp}$ ) polar caps are smaller than or similar in size to many of the other models despite having a considerably higher  $\Phi_{PC}$ . The equation HH90 used to define the convection flow reversal circle is  $\theta_0 = -3.8^\circ + 8.48^\circ \Phi_{pc}^{0.1875}$ , similar to equations found in G. L. Siscoe (1982) and M. Hairston and Heelis (1990). Although this is not the same as the polar cap radius proxy we have chosen to represent the size of the polar cap (Equation 11), it provides an estimate of how big the defined HH90 radius can be (see Figure S6 in Supporting Information S1). No other model is restricted by this equation; they can have larger polar cap radii per  $\Phi_{PC}$  than HH90. The expanding-contracting polar cap (ECPC) paradigm (G. Siscoe & Huang, 1985; Lockwood & Cowley, 1992; Milan et al., 2007) defines the rate of change of open flux in the polar ionosphere as the difference between dayside and nightside reconnection rates. Open flux increases when dayside reconnection exceeds nightside reconnection and decreases when nightside reconnection exceeds dayside reconnection. While the dayside reconnection rate is directly related to interplanetary conditions, the nightside rate is only weakly related to the IMF; it is dependent on the magnetic shear across the magnetotail current sheet (Lockwood et al., 2009). Therefore whilst it is likely that a large  $\Phi_{PC}$  will be associated with an increased polar cap size, it cannot be directly attributable. A large  $\Phi_{PC}$  driven equally by dayside and nightside reconnection would not impact the size of the polar cap, and a large  $\Phi_{PC}$  driven predominantly by nightside reconnection would cause the size of the polar cap to shrink.

As with the polar cap boundary variation, the LLBs are also highly variable. HH90 does not have a strict LLB as it is an exponentially decreasing function equatorward of the convection reversal boundary. However, we define a potential magnitude that provides an estimate of where the boundary would be (equivalent to the W05 mean potential at the HMB at midnight). Figure 5 shows that HH90 does not have  $|EF| > 25$  mV/m in the north-south component below  $60^\circ$  magnetic latitude at dawn or dusk, or at midnight or noon at any point during our time interval; all other models have  $|EF| > 25$  mV/m below  $60^\circ$  magnetic latitude. However in Figures 2 and 7, HH90 has a lower boundary similar to or lower than the other models during the main phase of the storm. In terms of the HMB, WGS21 has similar limits to TS18, despite its saturation. W05 and Map Potential extend  $\sim 10^\circ$  lower than WGS21 and TS18 during the main phase. Part of this may be due to the issues with poor HMB placement using the current algorithm within Map Potential (Fogg et al., 2020).

The shape of the convection cell from HH90 is also worth mentioning. The zero potential lines at midnight and noon are defined solely by the value of IMF  $B_y$ . The convection cells cannot overlap in MLT so this line is critical to the shape and longitudinal spread of the dawn and dusk cells. AENeAS hard codes limits of  $-11 \leq B_y \leq 7$  nT to restrict the placement of the zero potential line in the northern hemisphere to stop the pattern rotating excessively and the potential at the center of the pattern having a higher potential than the maximum and minimum values seen at the center of the convection cells. However, this presents further problems with these defined boundaries during times of strong IMF  $B_y$ . It is clear from the snapshots in Figure 3 that large changes in  $B_y$  have a significant effect on the rotation of the HH90 convection pattern, a rotation that is not obvious in the other models. In terms of the north-south component of the EF, small changes in IMF  $B_y$  result in sign changes in the EF measured at noon and midnight. This effect is highlighted in Figure S5 in Supporting Information S1. Figure 5 further highlights the problems with the fixed boundary at 24:00 MLT. The EF switches from strongly positive to strongly negative, and vice-versa, due to longitudinal changes in the location of the zero potential line that are purely a function of  $B_y$  variability. If  $B_y = 0$ , the zero potential line enters at 23.5 hr MLT, with negative  $B_y$  rotating it clockwise, and positive  $B_y$  rotating it anti-clockwise, by 0.15 hr per nT. When  $B_y < 0.3$  nT the direction of the EF bands switch.

The differences in both the size of the polar cap and the latitude of the LLB between the different models are important as they will have knock on effects in atmospheric models like AENeAS. For example, if a model places the LLB at too high a latitude then a region will be predicted to have zero EF instead of a non-zero EF and this will impact Joule heating estimates. The effects on Joule heating are less straightforward in terms of the radius of convection reversal (for which we use the polar cap radius proxy,  $r_{pc}$ ) but it is possible to envisage a situation where, if  $r_{pc}$  is changing, the EF direction is likely to be switching (as the boundary moves above and below a given geographical region). We know from Deng et al. (2009) that EF variability (and not just magnitude) is key to Joule heating.

## 5. Conclusions

Models of the high-latitude ionospheric EF are commonly used to specify the magnetospheric forcing in modern atmosphere models. The use of decades-old spacecraft-based models is still widespread. This is due to the lack of newer models with newer spacecraft data. For example, NASA has not flown a mission with EF measurements since the early 80s. However, modern radar-derived EF models could improve forecasting functionally. We have compared the AENeAS version of the Heelis model (M. Hairston & Heelis, 1990; HAO, 2018; Heelis et al., 1982) referred to as HH90, the Weimer model (W05) (Weimer, 2005b), Thomas and Shepherd (TS18) (Thomas & Shepherd, 2018) and Walach and Grocott geomagnetic Storm model (WGS21) (Walach et al., 2021), as well as the SuperDARN Map Potential. Here we compare the EF models during the September 2017 storm, covering a range of solar wind and IMF conditions. We explore the relationships between the IMF conditions and model output parameters and find:

- TS18 consistently has the lowest electric potential output and does not expand to low latitudes during the September 2017 storm. This is primarily because the TS18 model was developed using data from the relatively benign solar cycle 24 and has only one ionospheric electric potential solution for a solar wind EF value  $E_{sw} > 3$  mV/m (for given IMF  $B_y$  and dipole tilt). Thus TS18 is not suitable for use in AENeAS during storm times. If this model could be extended using a much larger SuperDARN data set over multiple solar cycles then it might be possible to produce a more accurate model version.
- WGS21 is parameterized by storm phase timings, not IMF and SW conditions. This improves the time-variability of the outputs, which evolve steadily, consistent with the Map Potential outputs that enhance and decay continuously. In contrast, the convection models that respond to instantaneous IMF conditions can expand and contract too quickly. WGS21 output, however, misses details associated with the individual storm. This variability could be captured by introducing additional parameterization to WGS21. Like TS18, WGS21 was developed using data from solar cycle 24 and thus is biased to ionospheric electric potential solutions appropriate to weaker storms.
- HH90 is hugely dependent on the  $\Phi_{PC}$  proxy used as input. HH90 based on Kp (as used in AENeAS) has very poor temporal resolution which makes it unsuitable for many applications. To use HH90 requires a potential proxy that has been well tested in storm conditions.
- HH90 ( $\Phi_L$ ) is comparable to W05 in electric potential magnitude and convection pattern topology but the transpolar voltage differs by  $\sim 50\%$  during peak storm times. Further work is needed to investigate if/to what extent HH90 ( $\Phi_L$ ) and W05 are over-estimating during active conditions.

Based on these findings we conclude that the main difference between models is that the parameters of the spacecraft-based electric potential solutions are fit to a continuous function of the input control variables, whereas the SuperDARN-based solutions are averages for comparable observed input conditions (e.g., binned by  $E_{sw}$ , or time within the storm). Consequently, the spacecraft-based models are designed to extrapolate to extreme conditions even beyond those observed whereas the SuperDARN-based models are constrained to the conditions available within the data used to develop them. This causes the SuperDARN-based model metrics to reach an artificial limit for rare extreme conditions, such as the apparent saturation of the transpolar voltage at  $\sim 100$  kV. This is also exacerbated by the known systematic under-estimation of the ionospheric EF by high frequency radars due to the ionospheric refractive index being less than the assumption of unity and limits introduced by the low latitude extent of the SuperDARN radars (Gillies et al., 2009, 2010, 2011). However, whilst the spacecraft-based models have no such limits, their solutions have high uncertainty because they are based on limited data or are extrapolations beyond the observed range based on equations with different functional forms.

Consequently, we recommend that efforts to nowcast and forecast the thermosphere using ensemble models such as AENeAS include an analysis of the effects of the uncertainties in the underlying EF models. This could be achieved by comparing the degree of satellite drag predicted using such models to direct satellite drag observations. In addition, more work should be done in further developing ionospheric EF models during geomagnetic storms, especially by including more data from periods of high geomagnetic activity. A greater understanding of the relevant physics such as transpolar voltage saturation and the refractive index effect are needed to bring the model predictions closer together. The upcoming NASA GDC mission will provide new measurements, which will allow for another point of comparison. Whilst the lack of a true EF measurement with double-probes on the GDC mission will handicap this comparison, more data will nevertheless allow for new comparisons. Comparisons with numerical models, such as the Gorgon MHD model (Eggington et al., 2022) which has the

ability to produce ionospheric electric potential patterns, could also prove informative in future comparison studies.

## Data Availability Statement

The version of the Heelis model used for the analysis in this paper is taken from TIEGCM (Qian et al., 2014), a model within AENeAS (Elvidge & Angling, 2019; HAO, 2018). A full description of the code is included in the SI. A full version of TIEGCM code can be downloaded from <https://www.hao.ucar.edu/modeling/tgcm/download.php>. The W05 code was provided by D. Weimer. It is available as an IDL model (Weimer, 2019), but the version used in this paper is the Fortran 90 code used within TIEGCM and is available as part of the aforementioned download. TS18 is available using the “solve\_model” module as part of the Radar Software Toolkit (RST Version 4.6) (SuperDARN Data Analysis Working Group et al., 2021), available for download at <https://doi.org/10.5281/zenodo.801458>. Map Potential and WGS21 were processed using the “maptoefield” RST module to find the electric potential from the fit.map files. The Map Potential data processing is described fully in Walach et al. (2022) and we use the equivalent of their “D4” data set. This includes data from all the northern hemisphere radars, which were processed using a range gate limit from 800 to 2,000 km and the TS18 background model. Where there are data gaps, model vectors are infilled from the TS18 background model. WGS21 storm phases are available from Lancaster University's research archive (PURE), Ionospheric Electric Field Morphologies during Geomagnetic Storm Phases 2.0, <https://doi.org/10.17635/lancaster/researchdata/417>. Heppner-Maynard-Rich Electric Field Model 1990 available from [https://git.smce.nasa.gov/ccmc-share/model-webarchive/-/tree/main/Heppner-Maynard-Rich\\_Electric-Field-Model](https://git.smce.nasa.gov/ccmc-share/model-webarchive/-/tree/main/Heppner-Maynard-Rich_Electric-Field-Model). Sunspot data is from <https://www.sidc.be/silso/infosnmot> (downloaded 14 October 2021). NASA OMNI data is available at [http://omniweb.gsfc.nasa.gov/form/omni\\_min.html](http://omniweb.gsfc.nasa.gov/form/omni_min.html) (downloaded 19 January 2021). Conversion from magnetic coordinates to geographic is calculated using the AACGM-v2 library (Burrell et al., 2020; S. Shepherd, 2014). The SuperDARN data are available from the BAS SuperDARN data mirror <https://www.bas.ac.uk/project/superdarn>.

## Acknowledgments

We would like to thank the SWIMMR consortium members for useful discussions and D. Weimer for provision of the W05 model. The authors acknowledge the use of SuperDARN data. SuperDARN is a collection of radars funded by the national scientific funding agencies of Australia, Canada, China, France, Italy, Japan, Norway, South Africa, UK, and United States. The work presented in this paper was supported by Natural Environment Research Council Grants NE/V00283X/1 and NE/V002686/1 (LO, AG), NE/P001556/1 and NE/T000937/1 (AG, M-TW), and NE/V002732/1 (MML, GC, MPF, RMS).

## References

- Boyle, C., Reiff, P., & Hairston, M. (1997). Empirical polar cap potentials. *Journal of Geophysical Research*, 102(A1), 111–125. <https://doi.org/10.1029/96ja01742>
- Bristow, W. A., Topliiff, C., & Cohen, M. B. (2022). Development of a high-latitude convection model by application of machine learning to superdarn observations. *Space Weather*, 20(1), e2021SW002920. <https://doi.org/10.1029/2021sw002920>
- Bruinsma, S., Boniface, C., Sutton, E. K., & Fedrizzi, M. (2021). Thermosphere modeling capabilities assessment: Geomagnetic storms. *Journal of Space Weather and Space Climate*, 11, 12. <https://doi.org/10.1051/swsc/2021002>
- Burrell, A., van der Meeren, C., & Laundal, K. M. (2020). aburrell/aacgm2: Version 2.6.0. *Zenodo*. <https://doi.org/10.5281/zenodo.3598705>
- Chisham, G., Lester, M., Milan, S. E., Freeman, M. P., Bristow, W. A., Grocott, A., et al. (2007). A decade of the super dual auroral Radar Network (SuperDARN): Scientific achievements, new techniques and future directions. *Surveys in Geophysics*, 28(1), 33–109. <https://doi.org/10.1007/s10712-007-9017-8>
- Cousins, E., & Shepherd, S. (2010). A dynamical model of high-latitude convection derived from superdarn plasma drift measurements. *Journal of Geophysical Research*, 115(A12), A12329. <https://doi.org/10.1029/2010ja016017>
- Deng, Y., Maute, A., Richmond, A. D., & Roble, R. G. (2009). Impact of electric field variability on joule heating and thermospheric temperature and density. *Geophysical Research Letters*, 36(8), L08105. <https://doi.org/10.1029/2008gl036916>
- Dickinson, R. E., Ridley, E., & Roble, R. (1981). A three-dimensional general circulation model of the thermosphere. *Journal of Geophysical Research*, 86(A3), 1499–1512. <https://doi.org/10.1029/ja086ia03p01499>
- Dimmock, A. P., Rosenqvist, L., Hall, J.-O., Viljanen, A., Yordanova, E., Honkonen, I., et al. (2019). The GIC and geomagnetic response over Fennoscandia to the 7–8 September 2017 geomagnetic storm. *Space Weather*, 17(7), 989–1010. <https://doi.org/10.1029/2018sw002132>
- Drayton, R., Koustov, A., Hairston, M., & Villain, J.-P. (2005). Comparison of DMSP cross-track ion drifts and superdarn line-of-sight velocities. *Annales Geophysicae*, 23(7), 2479–2486. <https://doi.org/10.5194/angeo-23-2479-2005>
- Eggington, J. W., Coxon, J. C., Shore, R. M., Desai, R. T., Mejnertsen, L., Chittenden, J. P., & Eastwood, J. P. (2022). Response timescales of the magnetotail current sheet during a geomagnetic storm: Global mhd simulations. *Frontiers in Astronomy and Space Sciences*, 9, 966164. <https://doi.org/10.3389/fspas.2022.966164>
- Elvidge, S., & Angling, M. J. (2019). Using the local ensemble transform kalman filter for upper atmospheric modelling. *Journal of Space Weather and Space Climate*, 9, A30. <https://doi.org/10.1051/swsc/2019018>
- Farris, M., & Russell, C. (1994). Determining the standoff distance of the bow shock: Mach number dependence and use of models. *Journal of Geophysical Research*, 99(A9), 17681–17689. <https://doi.org/10.1029/94ja01020>
- Fogg, A., Lester, M., Yeoman, T., Burrell, A., Imber, S., Milan, S., et al. (2020). An improved estimation of SuperDARN Heppner-Maynard boundaries using AMPERE data. *Journal of Geophysical Research: Space Physics*, 125(5), e2019JA027218. <https://doi.org/10.1029/2019ja027218>
- Gillies, R., Hussey, G., Sofko, G., McWilliams, K., Fiori, R., Ponomarenko, P., & St.-Maurice, J.-P. (2009). Improvement of superdarn velocity measurements by estimating the index of refraction in the scattering region using interferometry. *Journal of Geophysical Research*, 114(A7), A12329. <https://doi.org/10.1029/2008ja013967>
- Gillies, R., Hussey, G., Sofko, G., Ponomarenko, P., & McWilliams, K. (2011). Improvement of HF coherent radar line-of-sight velocities by estimating the refractive index in the scattering volume using radar frequency shifting. *Journal of Geophysical Research*, 116(A1), A12329. <https://doi.org/10.1029/2010ja016043>

- Gillies, R., Hussey, G., Sofko, G., Wright, D., & Davies, J. (2010). A comparison of EISCAT and SuperDARN A-region measurements with consideration of the refractive index in the scattering volume. *Journal of Geophysical Research*, *115*(A6). <https://doi.org/10.1029/2009ja014694>
- Grocott, A., Badman, S. V., Cowley, S., Milan, S. E., Nichols, J. D., & Yeoman, T. K. (2009). Magnetosonic mach number dependence of the efficiency of reconnection between planetary and interplanetary magnetic fields. *Journal of Geophysical Research*, *114*(A7). <https://doi.org/10.1029/2009ja014330>
- Grocott, A., & Milan, S. E. (2014). The influence of IMF clock angle timescales on the morphology of ionospheric convection. *Journal of Geophysical Research: Space Physics*, *119*(7), 5861–5876. <https://doi.org/10.1002/2014ja020136>
- Grocott, A., Milan, S. E., Sato, N., Wild, J. A., Yeoman, T. K., & Yukimatu, A. S. (2010). Superposed epoch analysis of the ionospheric convection evolution during substorms: IMF  $B_y$  dependence. *Journal of Geophysical Research*, *115*(A5), A00106. <https://doi.org/10.1029/2010JA015728>
- Grocott, A., Wild, J. A., Milan, S. E., & Yeoman, T. K. (2009). Superposed epoch analysis of the ionospheric convection evolution during substorms: Onset latitude dependence. *Annales Geophysicae*, *27*(2), 591–600. <https://doi.org/10.5194/angeo-27-591-2009>
- GSFC/SPDF, J., KingPapitashvili, N., & Systems, A. (2021a). *Omniweb: High resolution omni*. NASA. Retrieved from [https://omniweb.gsfc.nasa.gov/form/omni\\_min.html](https://omniweb.gsfc.nasa.gov/form/omni_min.html)
- GSFC/SPDF, J., KingPapitashvili, N., & Systems, A. (2021b). *One min and 5-min solar wind data sets at the earth's bow shock nose*. NASA. Retrieved from [https://omniweb.gsfc.nasa.gov/html/omni\\_min\\_data.html](https://omniweb.gsfc.nasa.gov/html/omni_min_data.html)
- Haaland, S., Paschmann, G., Förster, M., Quinn, J., Torbert, R., McIlwain, C., et al. (2007). High-latitude plasma convection from cluster EDI measurements: Method and IMF-dependence. *Annales Geophysicae*, *25*(1), 239–253. <https://doi.org/10.5194/angeo-25-239-2007>
- Hairston, M., & Heelis, R. (1990). Model of the high-latitude ionospheric convection pattern during southward interplanetary magnetic field using DE 2 data. *Journal of Geophysical Research*, *95*(A3), 2333–2343. <https://doi.org/10.1029/ja095ia03p02333>
- Hairston, M. R., Drake, K. A., & Skoug, R. (2005). Saturation of the ionospheric polar cap potential during the October–November 2003 superstorms. *Journal of Geophysical Research*, *110*(A9), A09S26. <https://doi.org/10.1029/2004ja010864>
- HAO (2018). TIEGCM v1.94 model description. Retrieved from [https://www.hao.ucar.edu/modeling/tiecm/doc/description/model\\_description.pdf](https://www.hao.ucar.edu/modeling/tiecm/doc/description/model_description.pdf)
- Heelis, R., Lowell, J. K., & Spiro, R. W. (1982). A model of the high-latitude ionospheric convection pattern. *Journal of Geophysical Research*, *87*(A8), 6339–6345. <https://doi.org/10.1029/ja087ia08p06339>
- Heppner, J., & Maynard, N. (1987). Empirical high-latitude electric field models. *Journal of Geophysical Research*, *92*(A5), 4467–4489. <https://doi.org/10.1029/ja092ia05p04467>
- Heppner, J. P. (1977). Empirical models of high-latitude electric fields. *Journal of Geophysical Research*, *82*(7), 1115–1125. <https://doi.org/10.1029/ja082i007p01115>
- Khan, H., & Cowley, S. (1999). Observations of the response time of high-latitude ionospheric convection to variations in the interplanetary magnetic field using EISCAT and IMP-8 data. *Annales Geophysicae*, *17*(10), 1306–1335. <https://doi.org/10.1007/s00585-999-1306-8>
- Kubota, Y., Nagatsuma, T., Den, M., Tanaka, T., & Fujita, S. (2017). Polar cap potential saturation during the Bastille Day storm event using global MHD simulation. *Journal of Geophysical Research: Space Physics*, *122*(4), 4398–4409. <https://doi.org/10.1002/2016ja023851>
- Liu, H.-L., Bardeen, C. G., Foster, B. T., Lauritzen, P., Liu, J., Lu, G., et al. (2018). Development and validation of the Whole Atmosphere Community Climate Model with thermosphere and ionosphere extension (WACCM-X 2.0). *Journal of Advances in Modeling Earth Systems*, *10*(2), 381–402. <https://doi.org/10.1002/2017ms001232>
- Lockwood, M., & Cowley, S. (1992). Ionospheric convection and the substorm cycle. In *Substorms I, proceedings of the first international conference on substorms, ICS-1* (Vol. 99–109).
- Lockwood, M., Hairston, M., Finch, I., & Rouillard, A. (2009). Transpolar voltage and polar cap flux during the substorm cycle and steady convection events. *Journal of Geophysical Research*, *114*(A1), A01210. <https://doi.org/10.1029/2008ja013697>
- Lockwood, M., & McWilliams, K. A. (2021). On optimum solar wind-magnetosphere coupling functions for transpolar voltage and planetary geomagnetic activity. *Journal of Geophysical Research: Space Physics*, *126*(12), e2021JA029946. <https://doi.org/10.1029/2021ja029946>
- Lomidze, L., Burchill, J. K., Knudsen, D. J., Kouznetsov, A., & Weimer, D. R. (2019). Validity study of the swarm horizontal cross-track ion drift velocities in the high-latitude ionosphere. *Earth and Space Science*, *6*(3), 411–432. <https://doi.org/10.1029/2018ea000546>
- Milan, S., Gosling, J., & Hubert, B. (2012). Relationship between interplanetary parameters and the magnetopause reconnection rate quantified from observations of the expanding polar cap. *Journal of Geophysical Research*, *117*(A3), 3226. <https://doi.org/10.1029/2011ja017082>
- Milan, S., Provan, G., & Hubert, B. (2007). Magnetic flux transport in the Dungey cycle: A survey of dayside and nightside reconnection rates. *Journal of Geophysical Research*, *112*(A1), A01209. <https://doi.org/10.1029/2006ja011642>
- Pettigrew, E., Shepherd, S., & Ruohoniemi, J. (2010). Climatological patterns of high-latitude convection in the northern and southern hemispheres: Dipole tilt dependencies and interhemispheric comparisons. *Journal of Geophysical Research*, *115*(A7), A07305. <https://doi.org/10.1029/2009ja014956>
- Qian, L., Burns, A. G., Emery, B. A., Foster, B., Lu, G., Maute, A., et al. (2014). The NCAR TIE-GCM: A community model of the coupled thermosphere/ionosphere system. *Modeling the ionosphere-thermosphere system*, *201*, 73–83. <https://doi.org/10.1002/9781118704417.ch7>
- Reiff, P., Spiro, R., Wolf, R., Kamide, Y., & King, J. (1985). Comparison of polar cap potential drops estimated from solar wind and ground magnetometer data: CDAW 6. *Journal of Geophysical Research*, *90*(A2), 1318–1324. <https://doi.org/10.1029/ja090ia02p01318>
- Reiff, P. H., Spiro, R. W., & Hill, T. (1981). Dependence of polar cap potential drop on interplanetary parameters. *Journal of Geophysical Research*, *86*(A9), 7639–7648. <https://doi.org/10.1029/ja086ia09p07639>
- Rich, F., & Maynard, N. (1989). Consequences of using simple analytical functions for the high-latitude convection electric field. *Journal of Geophysical Research*, *94*(A4), 3687–3701. <https://doi.org/10.1029/ja094ia04p03687>
- Richmond, A., & Kamide, Y. (1988). Mapping electrodynamic features of the high-latitude ionosphere from localized observations: Technique. *Journal of Geophysical Research*, *93*(A6), 5741–5759. <https://doi.org/10.1029/ja093ia06p05741>
- Ridley, A., & Kihn, E. (2004). Polar cap index comparisons with AMIE cross polar cap potential, electric field, and polar cap area. *Geophysical Research Letters*, *31*(7), L07801. <https://doi.org/10.1029/2003gl019113>
- Ruohoniemi, J., & Baker, K. (1998). Large-scale imaging of high-latitude convection with Super Dual Auroral Radar Network HF radar observations. *Journal of Geophysical Research*, *103*(A9), 20797–20811. <https://doi.org/10.1029/98ja01288>
- Ruohoniemi, J., & Greenwald, R. (1996). Statistical patterns of high-latitude convection obtained from Goose Bay HF radar observations. *Journal of Geophysical Research*, *101*(A10), 21743–21763. <https://doi.org/10.1029/96ja01584>
- Ruohoniemi, J., & Greenwald, R. (2005). Dependencies of high-latitude plasma convection: Consideration of IMF, seasonal, and UT factors in statistical patterns. *Journal of Geophysical Research*, *110*(A9), A09204. <https://doi.org/10.1029/2004ja010815>
- Shepherd, S. (2014). Altitude-adjusted corrected geomagnetic coordinates: Definition and functional approximations. *Journal of Geophysical Research: Space Physics*, *119*(9), 7501–7521. <https://doi.org/10.1002/2014ja020264>

- Shepherd, S., Greenwald, R., & Ruohoniemi, J. (2002). Cross polar cap potentials measured with super dual auroral radar network during quasi-steady solar wind and interplanetary magnetic field conditions. *Journal of Geophysical Research*, *107*(A7), SMP-5. <https://doi.org/10.1029/2001ja000152>
- Shepherd, S. G. (2007). Polar cap potential saturation: Observations, theory, and modeling. *Journal of Atmospheric and Solar-Terrestrial Physics*, *69*(3), 234–248. <https://doi.org/10.1016/j.jastp.2006.07.022>
- Shue, J.-H., Chao, J., Fu, H., Russell, C., Song, P., Khurana, K., & Singer, H. (1997). A new functional form to study the solar wind control of the magnetopause size and shape. *Journal of Geophysical Research*, *102*(A5), 9497–9511. <https://doi.org/10.1029/97ja00196>
- Siscoe, G., & Huang, T. (1985). Polar cap inflation and deflation. *Journal of Geophysical Research*, *90*(A1), 543–547. <https://doi.org/10.1029/ja090ia01p00543>
- Siscoe, G. L. (1982). Polar cap size and potential: A predicted relationship. *Geophysical Research Letters*, *9*(6), 672–675. <https://doi.org/10.1029/gi009i006p00672>
- SuperDARN Data Analysis Working Group, Schmidt, M., Bland, E., Thomas, E., Burrell, A., Coco, I., et al. (2021). SuperDARN/rst: RST 4.6. *Zenodo*. <https://doi.org/10.5281/zenodo.5156752>
- Thomas, E. G., & Shepherd, S. G. (2018). Statistical patterns of ionospheric convection derived from mid-latitude, high-latitude, and polar super-DARN HF radar observations. *Journal of Geophysical Research: Space Physics*, *123*(4), 3196–3216. <https://doi.org/10.1002/2018ja025280>
- Volland, H. (1975). Models of the global electric fields within the magnetosphere. *Annales Geophysicae*, *31*, 159–173.
- Walach, M.-T., & Grocott, A. (2019). SuperDARN observations during geomagnetic storms, geomagnetically active times, and enhanced solar wind driving. *Journal of Geophysical Research: Space Physics*, *124*(7), 5828–5847. <https://doi.org/10.1029/2019ja026816>
- Walach, M.-T., Grocott, A., & Milan, S. E. (2021). Average ionospheric electric field morphologies during geomagnetic storm phases. *Journal of Geophysical Research: Space Physics*, *126*(4), e2020JA028512. <https://doi.org/10.1029/2020ja028512>
- Walach, M.-T., Grocott, A., Staples, F., & Thomas, E. G. (2022). Super dual auroral radar network expansion and its influence on the derived ionospheric convection pattern. *Journal of Geophysical Research: Space Physics*, *127*(2), e2021JA029559. <https://doi.org/10.1029/2021ja029559>
- Weimer, D. (1995). Models of high-latitude electric potentials derived with a least error fit of spherical harmonic coefficients. *Journal of Geophysical Research*, *100*(A10), 19595–19607. <https://doi.org/10.1029/95ja01755>
- Weimer, D. (1996). A flexible, IMF dependent model of high-latitude electric potentials having “space weather” applications. *Geophysical Research Letters*, *23*(18), 2549–2552. <https://doi.org/10.1029/96gl02255>
- Weimer, D. (2001). An improved model of ionospheric electric potentials including substorm perturbations and application to the Geospace Environment Modeling November 24, 1996, event. *Journal of Geophysical Research*, *106*(A1), 407–416. <https://doi.org/10.1029/2000ja000604>
- Weimer, D. (2005a). Improved ionospheric electrodynamic models and application to calculating joule heating rates. *Journal of Geophysical Research*, *110*(A5), A05306. <https://doi.org/10.1029/2004ja010884>
- Weimer, D. (2005b). Predicting surface geomagnetic variations using ionospheric electrodynamic models. *Journal of Geophysical Research*, *110*(A12), A12307. <https://doi.org/10.1029/2005ja011270>
- Weimer, D. (2019). Weimer 2005 ionospheric electric potential model for IDL. *Zenodo*. <https://doi.org/10.5281/zenodo.2530324>
- Zhu, Q., Deng, Y., Maute, A., Kilcommons, L. M., Knipp, D. J., & Hairston, M. (2021). ASHLEY: A new empirical model for the high-latitude electron precipitation and electric field. *Space Weather*, *19*(5), e2020SW002671. <https://doi.org/10.1029/2020SW002671>